



ELSEVIER

Available online at www.sciencedirect.com

SCIENCE @ DIRECT®

Combustion and Flame 141 (2005) 448–468

Combustion
and Flame

www.elsevier.com/locate/combustflame

Gas phase chemistry in catalytic combustion of methane/air mixtures over platinum at pressures of 1 to 16 bar

Michael Reinke, John Mantzaras^{*}, Rolf Bombach, Sabine Schenker,
Andreas Inauen

Paul Scherrer Institute, Combustion Research, CH-5232 Villigen PSI, Switzerland

Received 18 November 2004; received in revised form 18 January 2005; accepted 26 January 2005

Available online 14 March 2005

Abstract

The gas-phase combustion of fuel-lean methane/air premixtures over platinum was investigated experimentally and numerically in a laminar channel-flow catalytic reactor at pressures $1 \text{ bar} \leq p \leq 16 \text{ bar}$. In situ, spatially resolved one-dimensional Raman and planar laser induced fluorescence (LIF) measurements over the catalyst boundary layer were used to assess the concentrations of major species and of the OH radical, respectively. Comparisons between measured and predicted homogeneous (gaseous) ignition distances have led to the assessment of the validity of various elementary gas-phase reaction mechanisms. At low temperatures ($900 \text{ K} \leq T \leq 1400 \text{ K}$) and fuel-to-air equivalence ratios ($0.05 \leq \varphi \leq 0.50$) typical to catalytic combustion systems, there were substantial differences in the performance of the gaseous reaction mechanisms originating from the relative contribution of the low- and the high-temperature oxidation routes of methane. Sensitivity analysis has identified the significance of the chain-branching reaction $\text{CHO} + \text{M} = \text{CO} + \text{H} + \text{M}$ on homogeneous ignition, particularly at lower pressures. It was additionally shown that C2 chemistry could not be neglected even at the very fuel-lean conditions pertinent to catalytic combustion systems. A gas-phase reaction mechanism validated at $6 \text{ bar} \leq p \leq 16 \text{ bar}$ has been extended to $1 \text{ bar} \leq p \leq 16 \text{ bar}$, thus encompassing all catalytic combustion applications. A reduced gas-phase mechanism was further derived, which when used in conjunction with a reduced heterogeneous (catalytic) scheme reproduced the key catalytic and gaseous combustion characteristics of the full hetero/homogeneous reaction schemes.

© 2005 The Combustion Institute. Published by Elsevier Inc. All rights reserved.

Keywords: Homogeneous combustion of methane over platinum; Reduced hetero/homogeneous reaction schemes; Catalytic combustion of methane; In situ Raman and LIF measurements

1. Introduction

The catalytic combustion of natural gas is actively pursued in many practical systems ranging from

atmospheric-pressure household burners and industrial boilers to medium-pressure (up to 6 bar) micro-turbines and, finally, to high-pressure ($\sim 16 \text{ bar}$) stationary gas turbines used for power generation. The latter employ the low- NO_x catalytically stabilized combustion (CST) technology [1,2], whereby about half of the fuel is converted heterogeneously (catalytically) and the remaining is combusted in a follow-up homogeneous (gaseous) burnout zone. The progress

^{*} Corresponding author. Fax: +41-56-3102199.

E-mail address: ioannis.mantzaras@psi.ch

(J. Mantzaras).

Nomenclature

b	channel half-height, Fig. 1	W_k, \bar{W}	gas-phase species molecular weight, average molecular weight
c_p	specific heat at constant pressure	X_k	gas-phase species mole fraction
D_{km}	mixture-average species diffusion coefficient, Eq. (7)	Y_k	gas-phase species mass fraction
D_k^T	species thermal diffusion coefficient, Eq. (7)	x, y, z	streamwise, transverse, and lateral physical coordinates, Fig. 1
h, h_k°	total enthalpy, chemical enthalpy of the k th gaseous species, Eq. (4)	<i>Greek symbols</i>	
k	reaction rate coefficient	Γ	surface site density, Eq. (6)
K_g	total number of gaseous species, Eq. (5)	θ_m	surface species coverage, Eq. (6)
M_s	total number of surface species, Eq. (6)	λ	thermal conductivity of gas, Eq. (4)
L	channel length, Fig. 1	μ	viscosity
p	pressure	ρ	density
R	universal gas constant	σ_m	surface species site occupancy, Eq. (6)
S	reactor surface, Eq. (11)	τ	reactor residence time, Eq. (11)
\dot{s}_k	heterogeneous molar production rate of k th species, Eq. (6)	τ_{ig}	ignition delay time
T, T_0	temperature and reference temperature, Eq. (8)	$\dot{\omega}_k$	homogeneous molar production rate of k th species, Eq. (5)
u, U_{IN}	streamwise velocity component, inlet streamwise velocity	<i>Subscripts</i>	
v	transverse velocity component	IN	inlet
\vec{V}_k	species diffusion velocity vector, Eq. (7)	k, m	indices for gas-phase and surface species
V	reactor volume, Eq. (11)	W	wall
W	channel width, Fig. 1	x, y	streamwise and transverse components

in catalytic combustion, particularly in the more demanding high-pressure systems, is largely dependent on crucial advances in catalyst technology (i.e., development of active and thermally stable catalysts) and in multidimensional numerical modeling needed for reactor design. Key to the aptness of the numerical models is the use of catalytic and of low-temperature gaseous chemical reaction schemes for methane (the main constituent of natural gas) that have been validated over the pressure, temperature, and composition ranges relevant to each particular application.

Appel et al. [3,4] and Reinke et al. [5] have recently introduced the methodology of in situ spatially resolved (across the boundary layer of a catalytic channel-flow reactor) Raman measurements of gas-phase species concentrations as a direct means to assess the catalytic reactivity at realistic operating conditions. The latter work [5] demonstrated the validity of the heterogeneous reaction scheme of Deutschmann et al. [6] for the total oxidation of fuel-lean CH_4/air mixtures over polycrystalline platinum at pressures $4 \text{ bar} \leq p \leq 16 \text{ bar}$. In conjunction with earlier atmospheric-pressure studies [6,7], the validity of the aforementioned scheme was ascertained over the entire pressure range of interest to practical systems. A reduced catalytic scheme based

on the elementary mechanism of Deutschmann et al. [6] and valid over the range $1 \text{ bar} \leq p \leq 16 \text{ bar}$ was further constructed in Reinke et al. [5]. More recently [4], the established experimental methodology has been extended to the partial catalytic oxidation of fuel-rich CH_4/air mixtures over rhodium at moderate pressures of 4 to 6 bar. Spatially resolved measurements of species concentrations were also reported over stagnation-flow boundary layers: Sidwell et al. [8,9] applied micro-probe sampling to study the atmospheric-pressure catalytic combustion of methane over hexaaluminates and Taylor et al. [10] used Raman to investigate the partial oxidation of methane over platinum at very low pressures ($p = 40 \text{ mbar}$).

Notwithstanding the large surface-to-volume ratios of monolithic honeycomb reactors that favor catalytic fuel conversion, the gaseous reaction pathway cannot always be ignored at elevated pressures [5]. Proper assessment of the gaseous chemistry necessitates experiments near a catalyst surface in order to capture the hetero/homogeneous chemistry coupling. The impact of this coupling on the homogeneous pathway is manifested by the near-wall catalytic reactant depletion that inhibits gas-phase combustion [11], the formation of heterogeneous products

(H₂O, CO₂) that inhibit or promote gaseous combustion [12–15], and, finally, the adsorption/desorption of minor radical species that promote/inhibit gas-phase ignition [14,16]. For the validation of gaseous reaction schemes, a suitable experimental approach is to monitor the concentration of a key radical, typically OH, using laser induced fluorescence (LIF). Most of the OH LIF studies over noble-metal surfaces have been performed at subatmospheric pressures and only a few at $p \geq 1$ bar: the latter were initiated by the $p = 1$ bar experiments of Cattolica and Schefer [17] and were followed by more recent measurements in the range $1 \text{ bar} \leq p \leq 16 \text{ bar}$ [12, 18–20]. It has been further established [3,13] that the combination of OH LIF and Raman measurements is well suited for the validation of gas-phase schemes; therein the homogeneous and heterogeneous pathways are assessed in parallel, hence eliminating uncertainties originating from the latter that could interfere with the evaluation of the former. Using this approach, homogeneous ignition studies were carried out in Appel et al. [3] (fuel-lean H₂/air mixtures, $p = 1$ bar) and Reinke et al. [13] (fuel-lean CH₄/air mixtures, $4 \text{ bar} \leq p \leq 16 \text{ bar}$). Reinke et al. [20] have additionally shown, encompassing earlier atmospheric-pressure studies [12], the validity of the gas-phase mechanism of Warnatz and Maas [21] in catalytic combustion of fuel-lean CH₄/air mixtures for $1 \text{ bar} \leq p \leq 6 \text{ bar}$; at the higher pressure range $6 \text{ bar} \leq p \leq 16 \text{ bar}$, however, the applicability of the gaseous scheme of Warnatz et al. [22] has been demonstrated [13]. Both gaseous schemes did not perform adequately outside their provided pressure ranges. A unique gas-phase scheme valid over the entire range $1 \text{ bar} \leq p \leq 16 \text{ bar}$ of interest to practical combustion systems has yet to be reported. Moreover, there is a clear need for the development of reduced homogeneous reaction schemes that can be coupled to (reduced) heterogeneous schemes for demanding computations in geometries of practical systems.

The present study undertakes an experimental and numerical investigation of fuel-lean CH₄/air catalytic combustion over Pt. Experiments were performed in an optically accessible catalytic channel-flow reactor, which was operated under steady and laminar conditions. The surface temperatures and pressures spanned the ranges $1050 \text{ K} \leq T \leq 1430 \text{ K}$ and $1 \text{ bar} \leq p \leq 16 \text{ bar}$, respectively. The atmospheric pressure data referred to an earlier study [12]; however, they were reevaluated using new kinetic schemes. Emphasis was given on new experiments in the transitional—for the scheme of Warnatz et al. [22]—range $1 \text{ bar} < p < 6 \text{ bar}$ (see also Table 1). One-dimensional Raman measurements provided the boundary layer profiles of major species and planar LIF of the OH radical monitored the onset of ho-

mogeneous ignition. Computations were carried out with an elliptic 2-D CFD code that included elementary catalytic and gaseous reaction schemes and detailed transport. The main objectives were to provide a gaseous scheme valid over the entire range $1 \text{ bar} \leq p \leq 16 \text{ bar}$ and then a reduced gaseous scheme, which (when coupled together with the validated heterogeneous scheme of Deutschmann et al. [6] or properly reduced catalytic schemes [5]) could reproduce key combustion characteristics such as gas-phase ignition and fuel conversion. Particular objectives were to investigate the effect of pressure on gaseous combustion and to elucidate the origin of the differences between various gas-phase mechanisms.

The experimental techniques and the numerical model are introduced first. The impact of the catalytic pathway is then elaborated, followed by detailed comparisons between OH LIF measurements and numerical predictions that lead to the assessment of the validity of various gas-phase mechanisms. Sensitivity and reaction flux analyses elucidate the differences among the gaseous schemes and lead to the construction of reduced gas-phase mechanisms.

2. Experimental

2.1. Reactor configuration and test conditions

The test rig has been used in earlier studies [5,20]; therefore, a brief description is provided below. It consisted of a channel-flow catalytic reactor, which formed a liner inside a high-pressure vessel (see Fig. 1). The reactor comprised two horizontal Si[SiC] ceramic plates (300 mm long (L), 110 mm wide, 9 mm thick, positioned 7 mm apart ($2b$)) and two vertical quartz glass windows (3 mm thick, 12 mm high, and 300 mm long). The lateral window separation was 104 mm (W) and the reactor volume was defined by the $300 \times 104 \times 7 \text{ mm}^3$ enclosure (Fig. 1); optical accessibility was available from both $300 \times 7 \text{ mm}^2$ reactor sides. The transverse reactor dimension ($2b$) was maintained by four 7-mm-high ceramic spacers affixed at the ceramic plate corners. The inner surfaces of the Si[SiC] plates were coated with a 2.2- μm -thick Pt layer on top of a nonporous 1.5- μm -thick Al₂O₃ layer. Both layers were applied with plasma vapor deposition (PVD). The thick Pt coating on a nonporous Al₂O₃ substrate closely resembled a polycrystalline platinum surface. This was verified with independent BET surface area (Kr physisorption) and X-ray photoelectron spectroscopy (XPS) surface composition measurements [5]. BET has demonstrated that the total and active surface areas were the same (0.26 m²/g catalyst), whereas XPS (carried out before and after the combustion tests) indicated that bulk Al or Si did

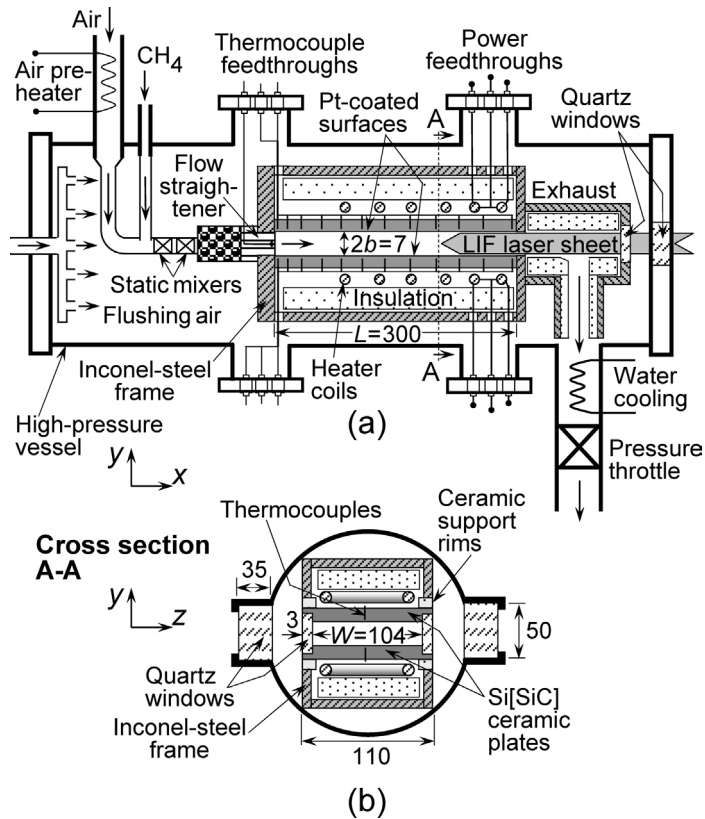


Fig. 1. Schematic of the high-pressure test rig and the catalytic reactor assembly; all distances are in mm.

not diffuse to the surface, which was only covered with Pt.

The surface temperature was monitored with 12 (for each plate) thermocouples placed along the x - y streamwise symmetry plane (Fig. 1) and embedded 0.9 mm beneath the catalyst, through 8.1-mm-deep holes eroded from the outer plate surfaces. Two adjustable-power resistive heating coils were positioned 15 mm above each ceramic plate, extending over $100 \text{ mm} \leq x \leq 300 \text{ mm}$; the external plate heating was of the utmost importance in attaining homogeneous ignition and this has to be contrasted to earlier pure heterogeneous kinetic studies [5] that required a water-cooling arrangement at the entry in order to maintain finite-rate surface chemistry. Regulation of both air and methane flows was achieved with calibrated Brooks mass-flow controllers, which yielded equivalence ratio accuracies better than $\pm 1\%$. Prior to mixing with methane, the air was preheated by a 3-kW electric heater. Two static Sulzer mixers (type SMV), a 40-mm-long packing of ceramic spheres, and a 40-mm-long inert ceramic honeycomb structure straightened the flow and assured uniform velocity, concentration, and temperature profiles at the reactor inlet. A thermocouple placed inside one channel of the inert honeycomb provided the inlet

temperature. The outer Si[SiC] plate surfaces were insulated with a porous fiber ceramic material and the reactor was mounted inside an inconel steel support frame. An insulated exhaust section, made also of inconel steel, directed the combustion products toward a water-cooled outlet of the high-pressure tank.

The high-pressure vessel was a 1.8-m-long and 0.28-m-inside-diameter cylindrical stainless-steel structure. Two 350-mm-long and 35-mm-thick quartz glass windows were mounted on the vessel, allowing optical access from both reactor sides (see Fig. 1b) and sustaining pressures up to 20 bar. Streamwise optical access for the LIF excitation beam (see discussion in Section 2.2) was attained via two additional quartz glass windows: one at the reactor exhaust and a second, 30-mm-thick high-pressure window, at the rear flange of the vessel (Fig. 1a). A continuous flow of flushing air removed any unwanted combustion products from the free volume between the vessel and the reactor assembly.

The laminar flow conditions are provided in Table 1. The atmospheric-pressure tests of Case 1 were performed in a shorter length reactor ($L = 250 \text{ mm}$) [12]. To avoid excessive surface temperatures that could endanger the catalyst integrity, the highest equivalence ratio was set to $\varphi = 0.40$. The

Table 1
Experimental conditions^a

Case	p (bar)	φ	U_{IN} (m/s)	T_{IN} (K)	Re_{IN}
1	1	0.31	1.00	754	170
2	2.4	0.40	0.68	556	473
3	3	0.36	0.75	560	640
4	4	0.36	0.54	566	599
5	6	0.36	0.43	569	717
6	8	0.36	0.38	587	797
7	10	0.40	0.30	572	824
8	12	0.40	0.62	635	1695
9	14	0.40	0.53	637	1694
10	16	0.40	0.45	643	1606

^a Pressure, equivalence ratio, inlet velocity, temperature, and Reynolds number.

lowest equivalence ratio ($\varphi = 0.31$) was determined by the requirement of attaining homogeneous ignition within the reactor. The Reynolds numbers of Table 1 were based on the uniform inlet properties and the channel hydraulic diameter ($=13.1$ mm); they were kept below 2000, even though the strong flow laminarization induced by the heat transfer from the hot catalytic plates guaranteed laminar flow conditions at considerably higher incoming Reynolds numbers [23].

2.2. Laser diagnostics

The planar LIF and Raman setup is depicted in Fig. 2. In the former experiment, the 532-nm second

harmonic radiation of an Nd:YAG pulsed laser (Quantel YG781C20) pumped a tunable dye laser (Quantel TDL50). The output of the dye laser was frequency-doubled to provide a 285-nm radiation with a pulse energy of 0.5 mJ, low enough to avoid saturation of the $A(v=1) \leftarrow X(v'=0)$ transition of the OH radical. The 285-nm beam was transformed into a thin laser sheet (using a cylindrical lens telescope and a 1-mm slit mask) that propagated counterflow along the x - y symmetry plane of the reactor (see Figs. 1a and 2). An intensified CCD camera (LaVision FlameStar 2F, 576×384 pixels) collected the fluorescence of both (1–1) and (0–0) transitions at 308 and 314 nm, respectively, through one pair of reactor and vessel side windows. A 120×7 mm² section of the channel was imaged on a 576×34 pixel area of the CCD; the camera was traversed axially to map the entire channel extent. Given the laminar and steady operating conditions, 400 single-shot LIF images were averaged to increase the signal-to-noise ratio. Calibration of the LIF was carried out with absorption measurements, whereby the laser beam crossed the reactor laterally (z) through the side windows, as reported in earlier studies [12,13,20].

In the spontaneous Raman experiments, the second harmonic radiation of the Nd:YAG laser provided the excitation source. A traversable mirror directed the 532-nm beam to the Raman or to the dye-laser/LIF setup (Fig. 2). Simultaneous acquisition of Raman and LIF data was not necessary given the steady and laminar flow operating conditions. The 532-nm

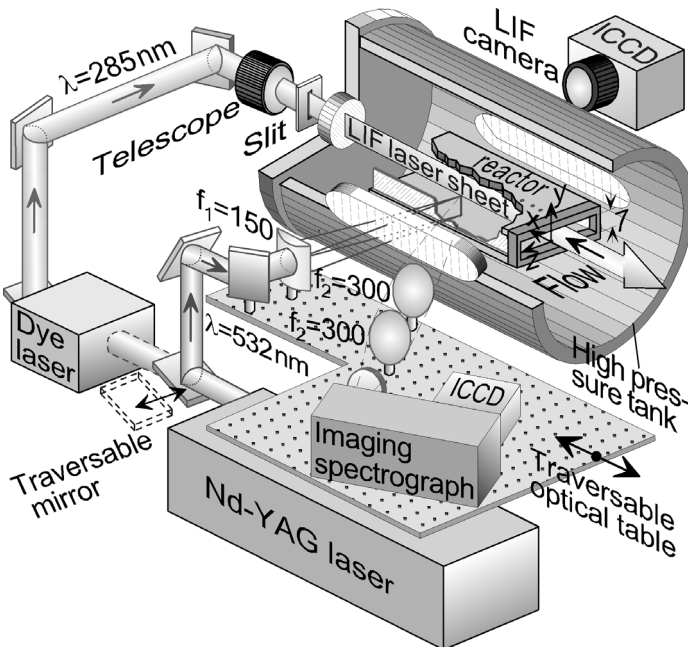


Fig. 2. Schematic of the Raman and the OH planar laser induced fluorescence (LIF) setup; all focal lengths are in mm.

beam was focused, through one pair of vessel and reactor side quartz windows, by an $f_1 = 150$ -mm cylindrical lens to a ~ 0.3 -mm-thick vertical line inside the reactor (Fig. 2). The focal line spanned the entire 7-mm transverse plate separation. To increase the light-collection angle and to minimize thermal beam steering, the focal line was laterally offset from the x - y symmetry plane ($z = 15$ mm) [3,5]. Two $f_2 = 300$ -mm spherical lenses collected the Raman-scattered light and focused it on the entrance slit of a 25-cm imaging spectrograph (Chromex 250i), which was equipped with an intensified CCD camera identical to that of the LIF setup; 2000 images were averaged to improve the signal-to-noise ratio. The 576×384 pixel dimension of the CCD camera corresponded to wavelength and transverse distance, respectively, and the 7-mm channel gap was resolved with 250 pixels. The effective Raman cross sections, which included transmission efficiencies, were evaluated by recording the signals of pure CH_4 , air, and completely burnt gases of known composition. Spectroscopic coefficients for the Raman cross section of CH_4 and H_2O were taken from Steiner [24] and Eisenberg [25], respectively. For the diatomic species, theoretical harmonic oscillator Raman cross section variations were used [26]. The sending and collecting optics were mounted on an axially traversable optical table that allowed Raman measurements over the extent $15.5 \text{ mm} \leq x \leq 163.5 \text{ mm}$. Raman measurements closer than 0.6 mm to both catalytic walls were disregarded due to low signal-to-noise ratios. The 250-pixel-long 7-mm transverse distance was binned to 63 pixels. Details of the Raman and the OH LIF experiments have been provided elsewhere [3,5,12,20].

3. Numerical model

3.1. Governing equations and boundary conditions for the 2-D channel model

An elliptic, two-dimensional, steady numerical model was used to simulate the channel experiments. The governing equations were as follows.

Continuity equation:

$$\frac{\partial(\rho u)}{\partial x} + \frac{\partial(\rho v)}{\partial y} = 0. \quad (1)$$

Momentum equations:

$$\begin{aligned} \frac{\partial(\rho uu)}{\partial x} + \frac{\partial(\rho vu)}{\partial y} + \frac{\partial p}{\partial x} \\ - \frac{\partial}{\partial x} \left[2\mu \frac{\partial u}{\partial x} - \frac{2}{3}\mu \left(\frac{\partial u}{\partial x} + \frac{\partial v}{\partial y} \right) \right] \\ - \frac{\partial}{\partial y} \left[\mu \left(\frac{\partial u}{\partial y} + \frac{\partial v}{\partial x} \right) \right] = 0, \end{aligned} \quad (2)$$

$$\begin{aligned} \frac{\partial(\rho uv)}{\partial x} + \frac{\partial(\rho vv)}{\partial y} + \frac{\partial p}{\partial y} - \frac{\partial}{\partial x} \left[\mu \left(\frac{\partial v}{\partial x} + \frac{\partial u}{\partial y} \right) \right] \\ - \frac{\partial}{\partial y} \left[2\mu \frac{\partial v}{\partial y} - \frac{2}{3}\mu \left(\frac{\partial u}{\partial x} + \frac{\partial v}{\partial y} \right) \right] = 0. \end{aligned} \quad (3)$$

Energy equation:

$$\begin{aligned} \frac{\partial(\rho uh)}{\partial x} + \frac{\partial(\rho vh)}{\partial y} + \frac{\partial}{\partial x} \left(\rho \sum_{k=1}^{K_g} Y_k h_k V_{k,x} - \lambda \frac{\partial T}{\partial x} \right) \\ + \frac{\partial}{\partial y} \left(\rho \sum_{k=1}^{K_g} Y_k h_k V_{k,y} - \lambda \frac{\partial T}{\partial y} \right) = 0. \end{aligned} \quad (4)$$

Gas phase species equations:

$$\begin{aligned} \frac{\partial(\rho u Y_k)}{\partial x} + \frac{\partial(\rho v Y_k)}{\partial y} + \frac{\partial}{\partial x} (\rho Y_k V_{k,x}) \\ + \frac{\partial}{\partial y} (\rho Y_k V_{k,y}) - \dot{\omega}_k W_k = 0, \\ k = 1, \dots, K_g. \end{aligned} \quad (5)$$

Surface species coverage equations:

$$\frac{\partial \theta_m}{\partial t} = \sigma_m \frac{\dot{s}_m}{\Gamma}, \quad m = 1, \dots, M_s. \quad (6)$$

In Eqs. (6), only the steady-state solutions were of interest. Buoyancy was not important for the relatively high Reynolds numbers of Table 1 and the narrow vertical channel gap (7 mm).

The species diffusion velocities \bar{V}_k were computed using mixture-average diffusion, including thermal diffusion for the light species [27]:

$$\bar{V}_k = -(D_{km}/Y_k) \nabla Y_k + (D_k^T/\rho Y_k T) \nabla T. \quad (7)$$

Finally, the ideal gas and caloric state laws closed the system of equations:

$$p = \frac{\rho RT}{\bar{W}} \quad \text{and} \quad h_k = h_k^0(T_0) + \int_{T_0}^T c_{p,k} dT. \quad (8)$$

The boundary conditions at the gas–wall interfaces ($y = 0$ and $y = 2b$) were

$$\begin{aligned} (\rho Y_k V_{k,y})_{y=0} = W_k (\dot{s}_k)_{y=0}, \\ (\rho Y_k V_{k,y})_{y=2b} = W_k (\dot{s}_k)_{y=2b} \end{aligned} \quad (9)$$

and

$$\begin{aligned} T(x, y = 0) = T_{W,L}(x), \\ T(x, y = 2b) = T_{W,U}(x), \end{aligned} \quad (10)$$

with $T_{W,L}(x)$ and $T_{W,U}(x)$ the thermocouple-measured temperature distributions of the lower and upper walls, respectively. No-slip boundary conditions were employed for both velocity components at the gas–wall interfaces. Uniform profiles for the inlet temperature T_{IN} (measured), the axial velocity U_{IN} (deduced

from the inlet temperature and the measured mass flow rates), and the species mass fractions were provided. Finally, $v = 0$ and zero-Neumann conditions for all other scalars were applied at the end of the computational domain ($x = 300$ mm). The governing equations were discretized using a finite volume approach and solution was obtained iteratively using a SIMPLER [28] method for the pressure–velocity field. Details on the solution algorithm have been provided elsewhere [14,29]. An orthogonal staggered grid of 350×120 points (in x and y , respectively) with finer x spacing toward the entrance and y spacing toward the wall was sufficient to produce a grid-independent solution.

In addition to the elliptic model, a simpler and computationally more efficient 2-D parabolic (boundary layer) model was used [30], with elementary hetero/homogeneous chemical reaction schemes and detailed transport. In the presence of homogeneous combustion, it has been demonstrated [30] that key parameters controlling the applicability of the parabolic model were the magnitude of the incoming velocity (U_{IN}) and the laminar flame speed (S_L) of the fresh mixture. Large U_{IN} and small S_L suppressed the upstream diffusion, rendering the parabolic approach valid. The low S_L of the present investigation (due to the fuel-lean incoming mixtures and the negative pressure dependence $S_{L,CH_4} \sim p^{-0.5}$) resulted in parabolic model predictions accurately reproducing those of the full elliptic model, at least for $p \geq 4$ bar. Therefore, the parabolic model was the preferred numerical tool for computationally intensive sensitivity analyses.

3.2. Ideal reactor modeling

The kinetic investigation was aided by additional computations in ideal reactors. The surface perfectly stirred reactor (SPSR) package of CHEMKIN [31] was used to simulate hetero/homogeneous combustion. The SPSR governing equations were as follows.

Gas-phase species equations:

$$-(1/\tau)(Y_k - Y_{k,IN}) + (1/\rho)[\dot{\omega}_k W_k + (S/V)\dot{s}_k W_k] = 0, \quad k = 1, \dots, K_g. \quad (11)$$

Energy equation:

$$-(1/\tau) \sum_{k=1}^{K_g} Y_{k,IN}(h_k - h_{k,IN}) - (1/\rho) \left[\sum_{k=1}^{K_g} h_k \dot{\omega}_k W_k \right. \\ \left. + (S/V) \sum_{k=1}^{K_g+M_s} h_k \dot{s}_k W_k \right] = 0, \quad (12)$$

with τ , S , and V the reactor residence time, surface, and volume, respectively. The surface coverage equations were provided by Eqs. (6) and the ideal gas laws by Eqs. (8). In the absence of surface reactions ($\dot{s}_k = 0$), the model reduced to a perfectly stirred reactor (PSR) [32]. Finally, the SENKIN package [33] computed ignition delay times in a constant-pressure batch reactor with gas-phase chemistry. The governing equations were as follows.

Gas-phase species equations:

$$dY_k/dt = (1/\rho)\dot{\omega}_k W_k, \quad k = 1, \dots, K_g. \quad (13)$$

Energy equation:

$$c_p(dT/dt) - (1/\rho) \sum_{k=1}^{K_g} h_k \dot{\omega}_k W_k = 0. \quad (14)$$

Equations (13) and (14), supplemented by the gas laws of Eqs. (8), were solved subject to proper initial conditions.

3.3. Chemical kinetics

The elementary heterogeneous scheme of Deutschmann et al. [6] (further referred to as Deutschmann) was used to describe the total oxidation of CH_4 over Pt. This scheme has been validated over the pressure and temperature ranges $4 \text{ bar} \leq p \leq 16 \text{ bar}$ and $780 \text{ K} \leq T \leq 1250 \text{ K}$ [5]; its applicability at atmospheric pressure has been demonstrated elsewhere [6,7]. The scheme consisted of 24 reactions and 11 surface and 9 gaseous species. A reduced catalytic reaction mechanism was also constructed in Reinke et al. [5] (13 reactions, 7 surface and 6 gaseous species) based on the full mechanism of Deutschmann. The reduced scheme is presented in Table 2 and will be further denoted as Deutschmann-R. A surface site density of $2.7 \times 10^{-9} \text{ mol/cm}^2$ was used in the numerical predictions, simulating a polycrystalline Pt surface [7,14], as discussed in Section 2.1. Surface thermochemical data were taken from Warnatz et al. [34].

Four different C1/H/O gas-phase mechanisms were investigated, which included the part of C2 chemistry that led to recombination of C1 radicals to C2 species. The mechanisms are further denoted as Warnatz-Maas [21] (18 species, 47 reversible and 11 irreversible reactions, including appropriate pressure dependencies for the reactions $CH_3 + H = CH_4$ and $CH_3 + CH_3 = C_2H_6$), Warnatz et al. [22] (25 species, 81 reversible and 27 irreversible reactions including appropriate pressure dependencies for the reactions $CH_3 + H = CH_4$, $CH_3 + CH_3 =$

Table 2
Reduced heterogeneous reaction scheme^a

		A (γ)	b	E
S1	$\text{CH}_4 + 5\text{Pt(s)} \rightarrow \text{C(s)} + 4\text{H(s)}$	0.01	0.0	0.0
S2	$\text{O}_2 + 2\text{Pt(s)} \rightarrow 2\text{O(s)}$	0.023	0.0	0.0
S3	$\text{O}_2 + 2\text{Pt(s)} \rightarrow 2\text{O(s)}$	$4.9\text{E}+12$	-0.5	0.0
S4	$\text{H}_2\text{O} + \text{Pt(s)} \rightarrow \text{H}_2\text{O(s)}$	0.75	0.0	0.0
S5	$\text{H(s)} + \text{O(s)} = \text{OH(s)} + \text{Pt(s)}$	$1.0\text{E}+13$	0.0	11.5
S6	$\text{OH(s)} + \text{OH(s)} = \text{H}_2\text{O(s)} + \text{O(s)}$	$1.0\text{E}+13$	0.0	48.2
S7	$\text{C(s)} + 2\text{O(s)} \rightarrow \text{CO}_2\text{(s)} + 2\text{Pt(s)}$	$1.0\text{E}+13$	0.0	62.8
S8	$2\text{O(s)} \rightarrow \text{O}_2 + 2\text{Pt(s)}$	$1.0\text{E}+13$	0.0	213.2–60 θ_0
S9	$\text{H}_2\text{O(s)} \rightarrow \text{H}_2\text{O} + \text{Pt(s)}$	$1.0\text{E}+13$	0.0	40.3
S10	$\text{CO}_2\text{(s)} \rightarrow \text{CO}_2 + \text{Pt(s)}$	$1.0\text{E}+13$	0.0	125.5
S11	$\text{OH} + \text{Pt(s)} \rightarrow \text{OH(s)}$	1.0	0.0	0.0
S12	$\text{OH(s)} \rightarrow \text{OH} + \text{Pt(s)}$	$1.0\text{E}+13$	0.0	192.8
S13	$\text{CO} + \text{O(s)} + \text{Pt(s)} \rightarrow \text{CO}_2\text{(s)} + \text{Pt(s)}$	0.84	0.0	0.0

^a The reduced scheme Deutschmann-R [5] was based on the full scheme of Deutschmann et al. [6]. Reaction rate coefficient $k = AT^b \exp(-E/RT)$. Units A (cm-mol-K-s), E (kJ/mol), except in the adsorption reactions S1, S2, S4, S11, and S13, whereby A denotes a sticking coefficient γ (-). S1 and S13 have a reaction order with respect to Pt(s) of 2.3 and 2, respectively. S7 and S13 have a reaction order with respect to O(s) of 1 and 0, respectively.

C_2H_6 , and $\text{CH}_3\text{OH} = \text{CH}_3 + \text{OH}$), GRI-3.0 [35] (26 species, 131 reversible and 6 irreversible reactions) and Leeds [36] (25 species, 105 reversible reactions). The species transport properties were calculated from the CHEMKIN database [27]. Each of the mechanisms in Refs. [22,35,36] was provided with its own thermodynamic data (Warnatz-Maas [21] had the same thermodata as Warnatz [22]). It is emphasized, however, that the discrepancies in the predictions with the above schemes (see next section) predominantly reflected kinetic and not thermodynamic differences; this was verified by interchanging the thermodynamic databases of the different mechanisms.

Gas-phase and surface reaction rates were evaluated using CHEMKIN [37] and Surface-CHEMKIN [38], respectively. A set of hetero/homogeneous schemes will be further denoted by the assigned names of its components, for example, Deutschmann/Warnatz schemes. Finally, the prefixes S and R will denote a surface and a gaseous reaction, respectively.

4. Results and discussion

4.1. Heterogeneous combustion

An assessment of the catalytic processes preceding the onset of homogeneous ignition is necessary before an evaluation of the gaseous schemes can be undertaken. Even though the scheme of Deutschmann [6] has been validated over the range $1 \text{ bar} \leq p \leq 16 \text{ bar}$, the relatively high surface temperatures required to achieve homogeneous ignition could possibly deactivate (totally or partially) the catalyst, leading to a near-wall fuel excess. Such fuel

excess could, in turn, promote the onset of homogeneous ignition [39] and hence falsify the gas-phase kinetics. It is emphasized that analytical homogeneous ignition criteria in channel-flow CST have shown [11] that there exist infinite combinations of catalytic and gaseous reactivities yielding exactly the same homogeneous ignition distance. Therefore, the Raman data removed any uncertainties associated with the heterogeneous pathway that could interfere with the evaluation of the gaseous chemistry.

Comparisons between measured and predicted (Deutschmann/Warnatz reaction schemes) transverse profiles of the CH_4 and H_2O mole fractions are given in Fig. 3 at three selected axial positions; for reasons of clarity only 28 of the 63 transverse measurement points are presented. The first two axial positions of Cases 4 and 6 and the first axial position of Case 10 (Figs. 3a, 3b, 3d, 3e, and 3g) were located far upstream of the homogeneous ignition position (measured or predicted using any of the four gaseous schemes, as will be discussed in the forthcoming Figs. 5 and 6). Therefore, the computations in Figs. 3a, 3b, 3d, 3e, and 3g were unaffected by the inclusion of (any) gaseous reaction scheme and reflected solely the contribution of the catalytic pathway. The very good agreement between measurements and predictions in the aforesaid axial positions demonstrated that the catalytic scheme realistically reproduced the underlying heterogeneous processes over the pressure and temperature range of this study. These processes were, in turn, crucial in determining the amount of fuel available for the follow-up homogeneous combustion. Typical measured axial temperature profiles are provided in Fig. 4. The upper and lower temperature profiles differed by as

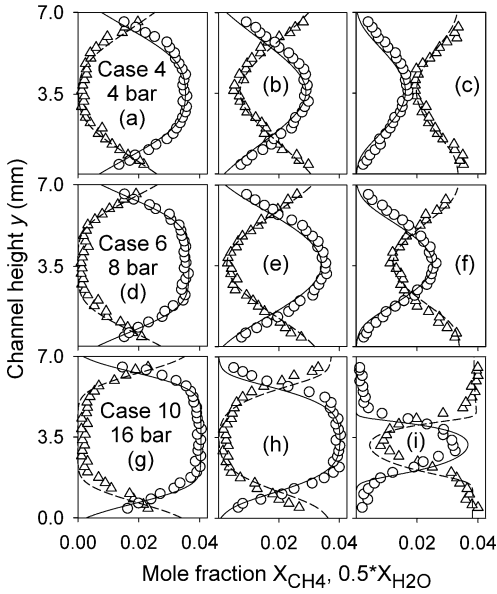


Fig. 3. Raman-measured (symbols) and numerically predicted (lines) transverse profiles of species mole fractions for three cases of Table 1: CH₄ (circles, solid lines); H₂O (triangles, dashed-lines). The corresponding axial positions are: (a, d, g) $x = 15.5$ mm, (b, e, h) $x = 53.5$ mm, (c, f) $x = 113.5$ mm, and (i) $x = 93.5$ mm. All predictions refer to the Deutschmann/Warnatz schemes.

much as 40 K, leading only to a slight asymmetry in the Raman profiles of Fig. 3. This was due to the nearly mass-transport-limited catalytic conversion of methane, which rendered the catalytic processes insensitive to small surface temperature variations. The mass-transport-limited operation was manifested by the very low predicted CH₄ levels near both walls (see Figs. 3a, 3b, 3d, 3e, and 3g). This behavior was also attested in the Raman measurements, despite the near-wall experimental limitations. The Raman data of H₂O complemented those of the limiting reactant (CH₄) since the production of the former was directly linked to the depletion of the latter: the near-wall zones were characterized by low CH₄ and high H₂O concentrations, whereas at the channel core the trend was reversed. This was particularly useful for the quantitative data assessment: the accuracy of the Raman measurements was as good as $\pm 4\%$ for species with volumetric compositions around 10%, dropping to $\pm 15\%$ for compositions as low as 0.5%.

The contribution of the gaseous pathway was non-negligible in Figs. 3c, 3f, and 3h even though they pertained to axial positions upstream of the homogeneous ignition point. The profiles in Fig. 3i were downstream the homogeneous ignition location and were greatly affected by the gaseous pathway, as manifested by the lack of CH₄ in extended zones near both

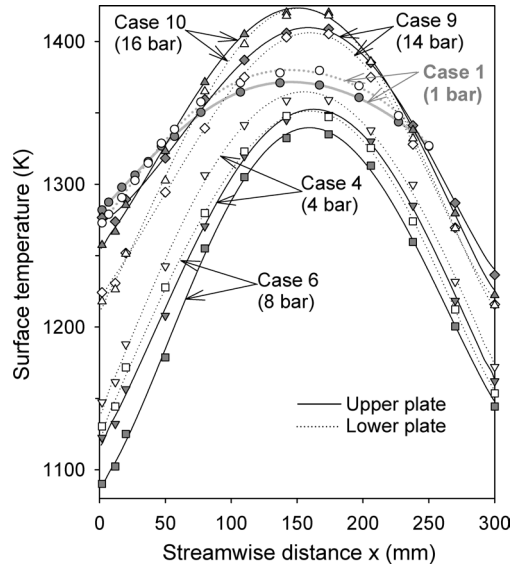


Fig. 4. Measured (symbols) axial surface temperatures for five selected cases of Table 1. Solid symbols, upper plate temperatures; open symbols, lower plate temperatures (Case 1, circles; Case 4, lower triangles; Case 6, squares; Case 9, diamonds; Case 10, upper triangles). The $p = 1$ bar case refers to earlier experiments in a 250-mm-long reactor [12]. Lines fitted through the measurements are also provided.

walls. Those issues will be elaborated in Sections 4.2 and 4.5.

4.2. Homogeneous ignition

Comparisons between LIF-measured and numerically predicted distributions of the OH radical are illustrated in Fig. 5 ($p \leq 4$ bar) and Fig. 6 ($p \geq 6$ bar). The heterogeneous scheme of Deutschmann [6] was used in all predictions. In the lower pressure flames of Fig. 5, computations with all four gaseous schemes were provided. In the higher pressure flames of Fig. 6, predictions with the scheme of Warnatz-Maas [21] were not included since the inapplicability of this scheme has been already established at $p > 6$ bar [20]. The stability of the ensuing V-shaped flames of Figs. 5 and 6 was excellent, allowing for detailed measurements over extended times. The flames of Figs. 5 and 6 exhibited a slight-to-moderate asymmetry depending on the temperature differences between the two catalytic walls (Fig. 4). Given the particular sensitivity of homogeneous ignition on the wall temperature [11,40], the asymmetries in the flames of Figs. 5 and 6 were more pronounced compared to those of the species transverse profiles (Fig. 3).

The location of homogeneous ignition (x_{ig}), shown with the green arrows in Figs. 5 and 6, was deter-

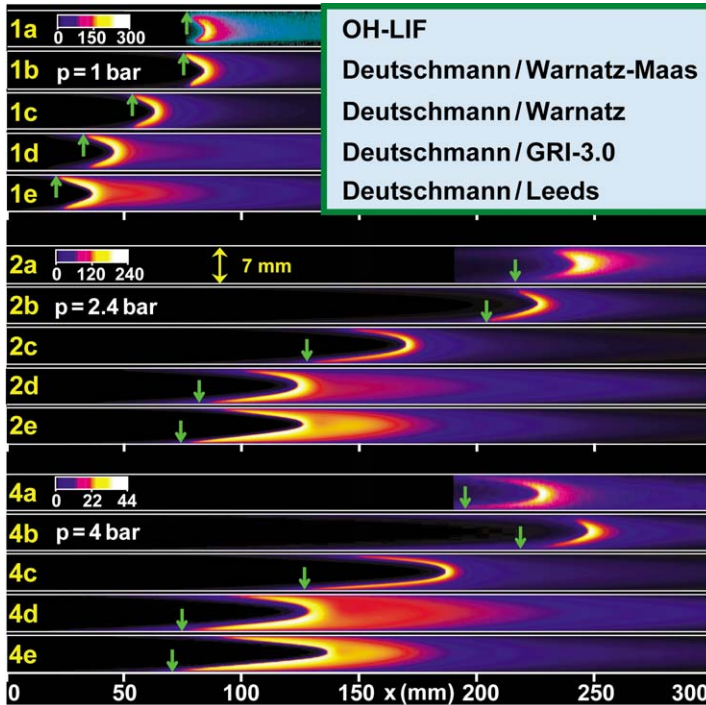


Fig. 5. Measured and predicted distributions of the OH radical for Cases 1, 2, and 4 of Table 1 ($p \leq 4$ bar). (a) OH LIF measurements and (b–e) numerical predictions with: (b) Deutschmann/Warnatz-Maas schemes, (c) Deutschmann/Warnatz schemes, (d) Deutschmann/GRI-3.0 schemes, and (e) Deutschmann/Leeds schemes. The green arrows define the onset of homogeneous ignition. The color bars provide the OH levels (ppmv) for the experiments and the Deutschmann/Warnatz-Maas and Deutschmann/Warnatz predictions.

mined by the intersection with the wall of a straight line fitted through the longer flame tail (i.e., the tail pertaining to the hotter wall). This definition was consistent with the sharp rise of OH along the reactor, as seen in the computed streamwise profiles of Fig. 7. Fig. 7 provides the averaged (over the 7-mm transverse distance) axial profiles of CH_4 , CO, and OH mole fractions as well as the fractional CH_4 conversion for three cases of Table 1. In the simulations of Fig. 7a the gaseous scheme of Warnatz-Maas [21] was used, while in the higher pressure cases of Figs. 7b and 7c the scheme of Warnatz [22] was employed. As seen in Fig. 7, the position of homogeneous ignition (x_{ig}) coincided with the sharp rise of the OH radical. The lower pressure flames (Fig. 5) had the highest absolute OH levels with their peak values relaxing rapidly in the postflame zones. The higher pressure flames (Fig. 6) had lower absolute OH levels that were, however, maintained over a longer postflame extent. The reason was the lower superequilibrium OH concentrations in the higher pressure flames due to the increased importance of three-body radical recombination reactions.

The capacity of the various gaseous reaction schemes to capture the homogeneous ignition dis-

tance (x_{ig}) was directly related to their aptness in correctly predicting ignition delay times; there was, nonetheless, the added complexity of the heterogeneous pathway (presence of catalytically produced major products and radical species in the induction zone). On the other hand, the postignition behavior of the gaseous schemes was linked to their ability to capture flame propagation characteristics (i.e., the sweep angle of the established flames). In catalytic combustion applications, the former requirement was far more important than the latter. Homogeneous ignition is considered detrimental to the catalyst integrity as it can cause catalyst meltdown. Hence, a numerical model used in reactor design should be able to predict, for safety reasons, the likelihood of such an event. Both distinct flame characteristics (ignition delay and flame propagation) could be assessed by planar OH LIF. Planar OH LIF alone could also provide indirect information on the validity of the catalytic reaction scheme: the postignition flame characteristics (flame sweep angle and absolute OH levels) bear the direct impact of the amount of fuel converted catalytically prior to homogeneous ignition. Therefore, in cases where the propagation characteristics of the gaseous scheme were already established, OH LIF

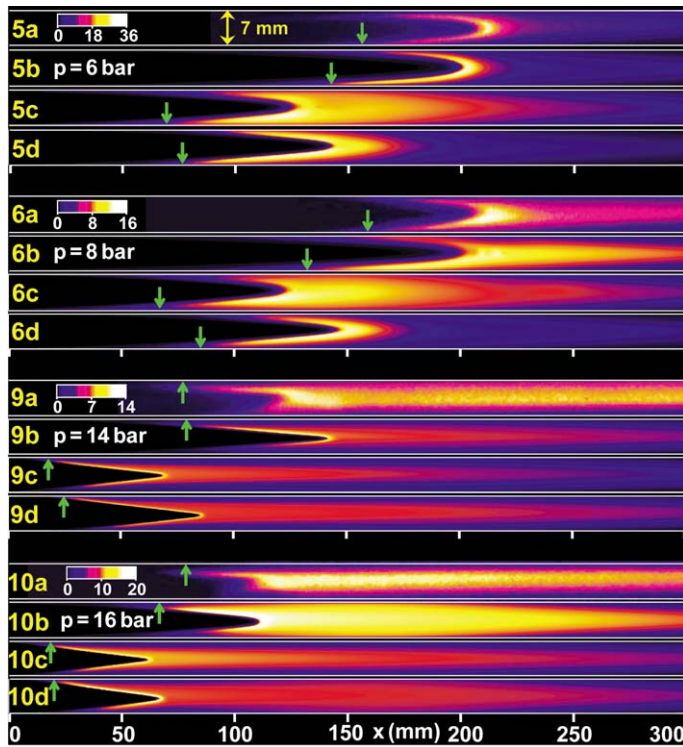


Fig. 6. Measured and predicted distributions of the OH radical for Cases 5, 6, 9, and 10 of Table 1 ($6 \text{ bar} \leq p \leq 16 \text{ bar}$). (a) OH LIF measurements and (b–d) numerical predictions with: (b) Deutschmann/Warnatz schemes, (c) Deutschmann/GRI-3.0 schemes, and (d) Deutschmann/Leeds schemes. The green arrows define the onset of homogeneous ignition. The color bars provide the OH levels (ppmv) for both the experiments and the Deutschmann/Warnatz predictions.

could be used for the validation of combined hetero/homogeneous reaction schemes (as in Dogwiler et al. [12]). Alternately, the Raman data alone could serve this purpose. For example, the Raman data of Fig. 3i (located downstream the measured onset of homogeneous ignition, $x_{\text{ig}} = 80 \text{ mm}$) showed a strong methane depletion in the near-wall zones that was indicative of gaseous combustion. Successive Raman species profiles could thus determine homogeneous ignition, albeit with a reduced accuracy compared to the planar OH LIF due to their discrete axial resolution.

Comparisons between measured and predicted homogeneous ignition characteristics are presented next. Having established in Section 4.1 the applicability of the catalytic scheme of Deutschmann [6], Figs. 5 and 6 provided direct validation for the gaseous mechanisms. The Deutschmann/Warnatz-Maas schemes captured well the measured flame shapes and the OH levels over the pressure range $1 \text{ bar} \leq p \leq 4 \text{ bar}$ (Fig. 5). In addition, they underpredicted the measured x_{ig} at $p = 1 \text{ bar}$ and 2.4 bar by only 2 and 5%, respectively, and overpredicted mildly (by 11%) the measured x_{ig} at $p = 4 \text{ bar}$. At $p > 6 \text{ bar}$, however, the above schemes resulted in

an appreciable overprediction of x_{ig} , as discussed in Reinke et al. [20]. Thus, the scheme of Warnatz-Maas [21] was suitable only for medium pressure systems (e.g., micro-turbines). In the higher pressure range $6 \text{ bar} \leq p < 16 \text{ bar}$, the Deutschmann/Warnatz schemes provided very good agreement to the measured x_{ig} (by 9–15%) as well as to flame shapes (Fig. 6). Over the pressure range $1 \text{ bar} \leq p \leq 4 \text{ bar}$, however, the Deutschmann/Warnatz schemes resulted in a significant underprediction of x_{ig} (by 22–40%). Finally, GRI-3.0 [35] and Leeds [36] provided much more pronounced underpredictions of x_{ig} (by 43–80%) at all pressures (Figs. 5 and 6). Both GRI-3.0 and Leeds gave similar predictions, the former yielding somewhat larger x_{ig} underpredictions at $p \geq 6$ and the latter at $p \leq 4 \text{ bar}$.

4.3. Comparisons between different gaseous reaction mechanisms

The origin of the differences between the gaseous reaction schemes is elaborated next. A first understanding of those differences is obtained with a comparison of ignition delay times, which were computed at fixed pressures and temperatures using the

SENKIN package [33]. The fixed temperature mimicked the presence of the heterogeneous pathway, which supplied heat to the flowing gas through the

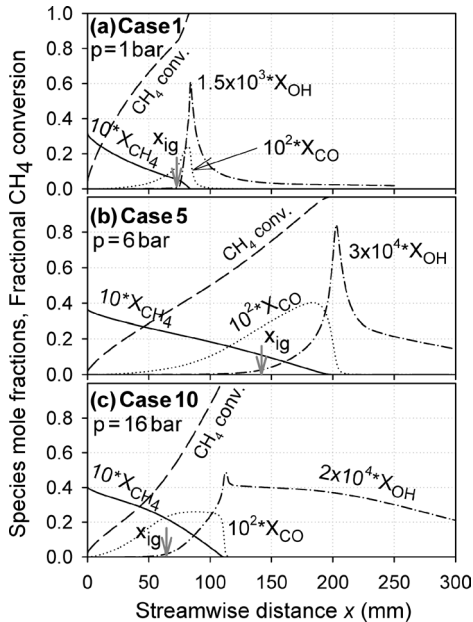


Fig. 7. Computed streamwise profiles of the averaged (over the transverse distance) mole fractions of CH_4 (solid lines), OH (dashed-dotted lines), and CO (dotted lines) for three cases of Table 1. Streamwise profiles of the fractional CH_4 conversions (due to both catalytic and gaseous pathways) are shown in dashed lines. The predictions refer to: (a) the Deutschmann/Warnatz-Mass schemes, and (b, c) the Deutschmann/Warnatz schemes. The arrows indicate the computed position of homogeneous ignition (x_{ig}).

hot catalytic walls. Predicted gas-phase ignition delay times τ_{ig} (from the solution of Eqs. (13), defined as the times corresponding to 50% methane conversion) versus φ are presented in Fig. 8 for the four schemes under investigation. Equivalence ratios as low as 0.05 were examined: such low values were relevant to practical systems due to the significant catalytic fuel conversion preceding the onset of homogeneous ignition. For example, the fractional conversion plots of Figs. 7a, 7b, and 7c illustrated that at the position of homogeneous ignition (x_{ig}) the fractional CH_4 conversion was 80, 72, and 46%, respectively. Shock-tube experiments [41] have further established that methane self-inhibited its ignition over the parameter range $1250 \text{ K} \leq T \leq 2000 \text{ K}$, $3 \text{ bar} \leq p \leq 15 \text{ bar}$, and $0.45 \leq \varphi \leq 1.2$: the ignition delay times correlated as $\tau_{ig} \propto [\text{CH}_4]^\alpha$, the exponent α being always positive ($\alpha \approx 0.33$ [41]). However, the ranges relevant to catalytic combustion were $900 \text{ K} \leq T \leq 1400 \text{ K}$ and $\varphi \leq 0.5$. A qualitative assessment of ignition characteristics is carried out with the aid of Fig. 8. It is shown next that one important factor influencing the performance of the schemes is the extent of φ over which the self-inhibited ignition behavior of methane was maintained.

At $p = 1 \text{ bar}$, GRI-3.0 yielded always a self-inhibited ignition for all T and φ , as manifested by the positive slopes in the log–log plots of Fig. 8a. The same behavior was also attested at 6 bar ($T \geq 1100 \text{ K}$, $\varphi \geq 0.05$) and 16 bar ($T \geq 1300 \text{ K}$, $\varphi \geq 0.1$). The exponent α in GRI-3.0 ranged from 0.35–0.45 ($p = 1 \text{ bar}$, $T \geq 1100 \text{ K}$) to 0.25–0.38 ($p = 6 \text{ bar}$, $T \geq 1100 \text{ K}$) and to 0.20–0.25 ($p = 16 \text{ bar}$, $T \geq 1300 \text{ K}$). This resulted in a rapid and unrealistic acceleration

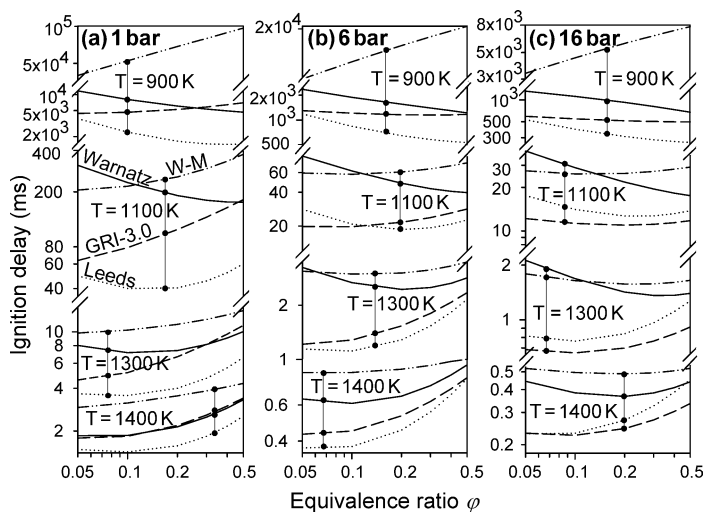


Fig. 8. Ignition delay times of CH_4/air mixtures at fixed pressures and temperatures calculated using four gas-phase mechanisms. Three pressures are presented with four temperatures for each pressure. Solid lines, Warnatz [22]; dashed lines, GRI-3.0 [35]; dotted lines, Leeds [36]; dashed double-dotted lines, Warnatz-Mass [21].

of the gaseous reactivity at ultralow φ , which was consistent with the significant x_{ig} underpredictions of GRI-3.0 in the channel (Figs. 5 and 6). Only at very low φ ($\varphi < 0.025$ at $p = 1$ bar, not shown in Fig. 8) the exponent α turned to negative, providing a decline of the gaseous reactivity with decreasing φ . A similar trend was observed with the Warnatz-Maas scheme, although the inhibition was moderate as illustrated by the generally smaller positive slopes of Fig. 8. At $p = 1$ bar, the exponent α decreased with increasing temperature, from ~ 0.43 ($T = 900$ K) to ~ 0.16 ($T = 1400$ K); at $p = 6$ and 16 bar and for $T \geq 1100$ K, the scheme exhibited an almost neutral behavior ($-0.04 \leq \alpha \leq 0.08$). In contrast to GRI-3.0 and Warnatz-Maas schemes, the scheme of Warnatz displayed self-inhibited ignition at $p = 1$ bar only for $T \geq 1300$ K and φ greater than a minimum value that decreased with increasing temperature. At higher pressures (6 and 16 bar) the trends were maintained, with the difference that the turnover from promotion ($\alpha < 0$) to inhibition ($\alpha > 0$) occurred at higher T . Over the regimes of φ with self-inhibited ignition and for $T = 1400$ K, the scheme of Warnatz yielded exponents α ranging from 0.35 to 0.25, in basic agreement with shock-tube measurements [41]. The good performance of Warnatz' scheme in the comparisons of Fig. 6 suggested that it captured correctly the p - T - φ parameter ranges of the self-inhibited ignition behavior of methane at $p \geq 6$ bar. The scheme of Leeds showed the same trends with the scheme of Warnatz at $p = 1$ bar, although the self-inhibition was maintained always at lower φ for $T \geq 1100$ K. At $p = 6$ and 16 bar, on the other hand, Leeds gave trends similar to those of GRI-3.0. Finally, the discrepancies of Fig. 8 were predominantly kinetic: when interchanging the thermodynamic database of a given mechanism with the databases of the other mechanisms, the ignition delay predictions were altered by less than 12%.

The ignition characteristics were further investigated systematically using reaction flux and sensitivity analyses (SA). An SA of the gaseous chemistry on the homogeneous ignition distance x_{ig} is provided in Fig. 9 for the scheme of Warnatz. The preexponentials of all gaseous reactions were multiplied/divided by a factor of 2 and the x_{ig} in the channel were computed anew, while keeping the heterogeneous scheme of Deutschmann unaltered. The 10 most sensitive reactions affecting homogeneous ignition are shown in Fig. 9 for Case 1 (1 bar) and Case 10 (16 bar). Supplementary SA at intermediate pressures and with different multiplication/division factors produced the same set of significant reactions. The most sensitive reactions in the H/O subset were the chain-branching $O_2 + H = OH + O$ (R1) and chain-terminating steps $HO_2 + OH = H_2O + O_2$ (R2)

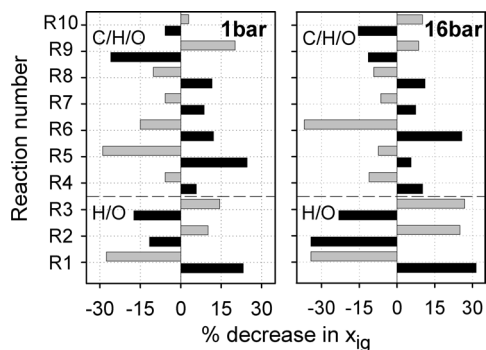


Fig. 9. Sensitivity analysis on the homogeneous ignition distance x_{ig} for the gaseous scheme of Warnatz [22]. The 10 most sensitive reactions affecting homogeneous ignition are shown for Case 1 (1 bar) and Case 10 (16 bar); the gray bars indicate division and black bars multiplication of the reaction preexponentials. The numbering of reactions is the same as in Table 4.

and $H + O_2 + M = HO_2 + M$ (R3). A similar SA for the GRI-3.0, Warnatz-Maas, and Leeds schemes revealed the same group of important reactions in the H/O subset. Exchanging the full H/O subset in the schemes of GRI-3.0 and Leeds (Warnatz-Maas and Warnatz had nearly identical H/O subsets) with the one of Warnatz shifted the onset of homogeneous ignition in Figs. 5 and 6 farther downstream by ~ 20 and $\sim 15\%$, respectively, improving somewhat the agreement with the LIF experiments. The same trends were also observed qualitatively in ignition delay computations under constant p and T . The differences in the H/O subset stemmed from the radical recombination reaction $HO_2 + OH = H_2O + O_2$ (R2): over the temperature range $900 \text{ K} \leq T \leq 1400 \text{ K}$, the R2 rate coefficient in Warnatz' scheme was ~ 3.0 and ~ 1.5 times larger compared to that of GRI-3.0 and Leeds, respectively.

A carbon reaction flux analysis is presented in Fig. 10 for $p = 1$ and 16 bar using a PSR model [32] and the scheme of Warnatz. Flux analyses at discrete axial positions in the channel reactor provided also the same set of important reaction pathways with those of Fig. 10. The fuel depletion was initiated by $CH_4 + OH = CH_3 + H_2O$ (R6). The main route for CH_3 consumption was the formation of formaldehyde $CH_3 + O_2 \rightarrow CH_2O + OH$ (R4), which was mainly a low-temperature pathway [42]. The high-temperature route to CH_3O [42] was less important: it proceeded predominantly via $CH_3 + HO_2 = CH_3O + OH$ (R8) and to a lesser extent via $CH_3 + O_2 = CH_3O + O$. In addition, at low pressures (< 4 bar) the $CH_3 \rightarrow CH_3OH \rightarrow CH_2OH \rightarrow CH_2O$ route was nonnegligible in the scheme of Warnatz at $p = 1$ bar (see Fig. 10a). On the other hand, GRI-3.0 had different oxidation pathways: the main route was via CH_3O

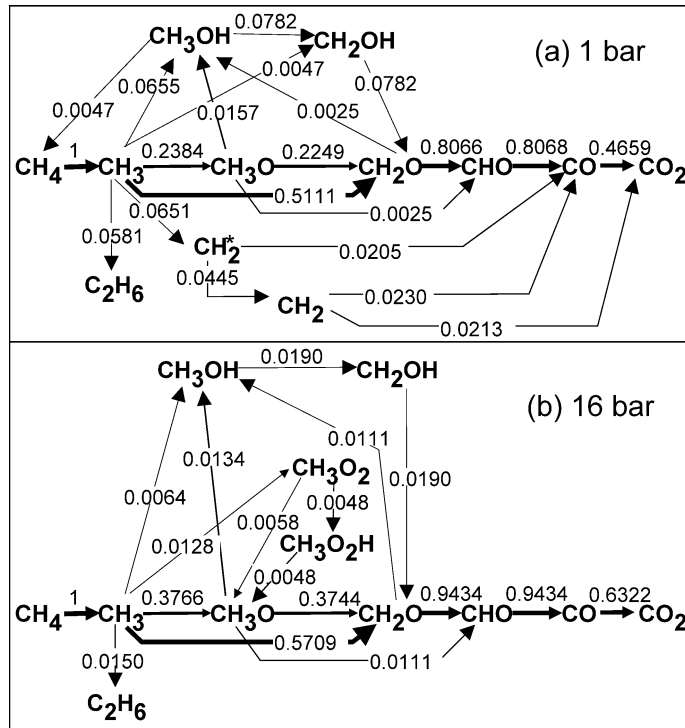


Fig. 10. Reaction flux of carbon for the gas-phase mechanism of Warnatz [22] computed with a perfectly stirred reactor (PSR): (a) $p = 1$ bar and (b) $p = 16$ bar. The residence time is 30 ms, $\varphi = 0.40$ and the temperature is 1200 K. All fluxes are normalized with respect to the $\text{CH}_4 \rightarrow \text{CH}_3$ flux. Fluxes lower than 0.002 are not shown.

formation (R8) and the route to CH_2O (R4) was much less important. Furthermore, R8 was accelerated by the slower HO_2 -depleting reaction R3 of the H/O subset. The scheme of Leeds favored CH_3 depletion via R4, however, the route to CH_3O had an increased importance compared to that of Warnatz. The aforementioned importance of the high- and low-temperature oxidation routes in the schemes of Warnatz, GRI-3.0, and Leeds was maintained over the entire range $900 \text{ K} \leq T \leq 1400 \text{ K}$ and $0.05 \leq \varphi \leq 0.5$. Finally, in the Warnatz-Maas scheme only the low-temperature oxidation route was available and the CH_3O route was not included. This could be a possible reason for the long ignition delay times of this scheme shown in Fig. 8. Additional radical (O, H, and OH) reaction flux analyses in the channel reactor have shown a stronger radical pool built up over the preignition zone for GRI-3.0 and Leeds compared to that of Warnatz' scheme. The dominant H radical source was reaction $\text{CHO} + \text{M} = \text{CO} + \text{H} + \text{M}$ (R5), while R1 and R4 were main sources for O and OH, respectively. Moreover, of the significant C-containing reactions in Warnatz' scheme, R5 had the strongest pressure dependence (see Fig. 9). Sensitivity analyses on the other schemes have also attested to the significance of R5 and its strong pressure dependency. R5 will

be elaborated in Section 4.4, where a modified reaction mechanism is constructed for $1 \text{ bar} \leq p \leq 16 \text{ bar}$. It is finally noted that the large differences of Fig. 8 were only particular to the intermediate temperatures $900 \text{ K} \leq T \leq 1400 \text{ K}$ relevant to catalytic systems; at $T = 1500$ and 1600 K , for example, the computed ignition delay times with the Warnatz, GRI-3.0, and Leeds schemes differed by less than 30% over the range $1 \text{ bar} \leq p \leq 16 \text{ bar}$ and $0.05 \leq \varphi \leq 0.5$.

The significance of C2 chemistry under the very fuel-lean catalytic combustion operation is an issue that deserves particular attention. In all examined mechanisms, the reactions involving recombination of C1 radicals to C2 species were considered as integral parts of the C1 mechanism. In Warnatz' scheme, for example, five C2 reactions were accounted for: $\text{CH}_3 + \text{CH}_3 = \text{C}_2\text{H}_6$, $\text{CH}_2 + \text{CH}_3 = \text{C}_2\text{H}_4 + \text{H}$, $\text{CH}_2(\text{s}) + \text{CH}_3 = \text{C}_2\text{H}_4 + \text{H}$, $\text{CH}_3 + \text{CH}_3 = \text{C}_2\text{H}_4 + \text{H}_2$ and $\text{CH}_4 + \text{CH} = \text{C}_2\text{H}_4 + \text{H}$. The resulting scheme of Warnatz (108 reactions, 25 species) produced ignition delay times (constant p and T) within 9% of those calculated using the full C2 mechanism of Warnatz (164 reactions, 33 species) over the entire parameter range $900 \text{ K} \leq T \leq 1400 \text{ K}$, $1 \text{ bar} \leq p \leq 16 \text{ bar}$, and $0.05 \leq \varphi \leq 0.5$. Exclusion of the above five reactions resulted in ignition de-

lay times appreciably shorter compared to those of the full C2 mechanism: by $\sim 20\%$ at 1100 K and by $\sim 80\%$ at 1400 K ($p = 4$ bar, $\varphi = 0.5$). At lower φ the discrepancies were less dramatic ($\sim 7\%$ at 1100 K and $\sim 26\%$ at 1400 K, $\varphi = 0.1$, $p = 4$ bar). With increasing pressure the differences were slightly reduced and the maximum deviation was shifted to higher temperatures. The most significant of the five C2-containing reactions was $\text{CH}_3 + \text{CH}_3 = \text{C}_2\text{H}_6$.

In GRI-3.0 12 C1-to-C2 reactions were included, resulting in a mechanism consisting of 137 reactions with 26 species. This scheme overpredicted the ignition delay times calculated with the full C3 chemistry of GRI-3.0 (219 reactions, 34 species) by less than 10% at $T \leq 1100$ K and by less than 16% at $1100 \text{ K} < T \leq 1400 \text{ K}$ ($p = 4$ bar, $0.05 \leq \varphi \leq 0.5$). Similar to the scheme of Warnatz, the overpredictions were slightly reduced with increasing pressure and shifted to higher temperatures. When all 12 C1-to-C2 reactions were removed, the ignition delay times were much shorter compared to those of the full C3 mechanism at $900 \text{ K} < T \leq 1400 \text{ K}$: up to 460% for $\varphi = 0.5$ and up to 200% for $\varphi = 0.05$ ($p = 4$ bar). At 16 bar, the corresponding differences were 350 and 160%. Again the most important C1-to-C2 reaction was $\text{CH}_3 + \text{CH}_3 = \text{C}_2\text{H}_6$. Finally, the C1 scheme of Leeds (105 reactions and 25 species) involved 15 C1-to-C2 reactions. Comparisons between the C1 and the C2 (125 reactions, 29 species) Leeds schemes revealed minor differences in ignition delay times. However, removing the C1-to-C2 reactions resulted in large ignition delay time discrepancies similar to those of GRI-3.0. Simulations with the scheme of Warnatz-Maas have also shown the—common to all schemes—importance of C1-to-C2 recombination reactions in catalytic combustion applications.

4.4. Modified mechanism valid between 1 and 16 bar

The good performance of the gaseous scheme of Warnatz over the extended domain $6 \text{ bar} \leq p \leq 16 \text{ bar}$ provided a platform for the establishment of a mechanism valid for the entire range $1 \text{ bar} \leq p \leq 16 \text{ bar}$. The analysis of Fig. 9 revealed that at $p = 1$ bar the homogeneous ignition was particularly sensitive to the chain-branching step $\text{CHO} + \text{M} = \text{CO} + \text{H} + \text{M}$ (R5) while at $p = 16$ bar the corresponding sensitivity was weak. Analyses at in-between pressures have further shown the decreasing sensitivity of R5 with increasing pressure. This behavior was attributed to the reverse reaction R5 which, as a three-body reaction, was favored at high pressures. The importance of R5 has also been attested in earlier atmospheric pressure studies [14]. Therefore, R5 could be a possible source for the large x_{ig} differences of Warnatz' scheme at $p \leq 4$ bar (Fig. 5). In the literature there

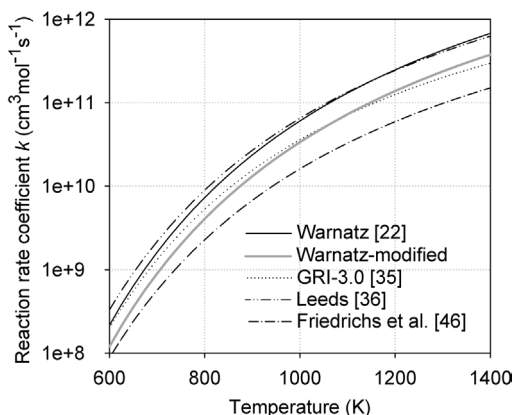


Fig. 11. Rate coefficient $k = AT^b \exp(-E/RT)$ for the reaction $\text{CHO} + \text{M} = \text{CO} + \text{H} + \text{M}$: Warnatz [22], solid lines; GRI-3.0 [35], dotted lines; Leeds [36], dashed double-dotted lines; Friedrichs [46], dashed-dotted lines. The Warnatz-modified rate (solid gray lines) has a reaction pre-exponential reduced by a factor of 1.8 compared to that of Warnatz [22].

is a large scatter of R5 kinetic parameters. Warnatz, Warnatz-Maas, and Leeds adapted their kinetic parameters from the data of Baulch et al. [43]. GRI-3.0 used the data of Timonen et al. [44], which were measured at $637 \leq T \leq 832 \text{ K}$ and were further extended to $300 \text{ K} \leq T \leq 3000 \text{ K}$ using a theoretical model. Glarborg et al. [45] in a recent study on formaldehyde oxidation recommend the latest kinetic data of Friedrichs et al. [46], which were extracted at $835 \text{ K} \leq T \leq 1230 \text{ K}$ and $0.28 \text{ bar} \leq p \leq 1.9 \text{ bar}$. The calculated rate coefficients $k_5 = AT^b \exp(-E/RT)$ are provided in Fig. 11. The kinetic parameters A , b , and E along with the bath gas used in the original kinetic experiments and the enhanced third-body efficiencies of the full mechanisms are listed in Table 3. The differences in k_5 span a factor of ~ 4 over the temperature range $600 \text{ K} \leq T \leq 1400 \text{ K}$.

To improve the homogeneous ignition predictions at $p \leq 4$ bar (Fig. 5), the pre-exponential of R5 in the scheme of Warnatz was reduced by a factor 1.8. The altered scheme is further denoted as Warnatz-modified. As seen in Fig. 11, the modified reaction rate coefficient is well within the range of literature values. This modification had little impact on the high-pressure performance of Warnatz' scheme, while it greatly improved its lower pressure ignition predictions. Comparisons between OH LIF measurements and numerical predictions with the Deutschmann/Warnatz and Deutschmann/Warnatz-modified schemes are presented in Fig. 12 (predictions referring to the reduced schemes will be elaborated in the next section). Over the range $1 \text{ bar} \leq p \leq 4 \text{ bar}$ the agreement in x_{ig} was improved to $\sim 10\%$ as seen, for example, in the $p = 1$ bar comparisons

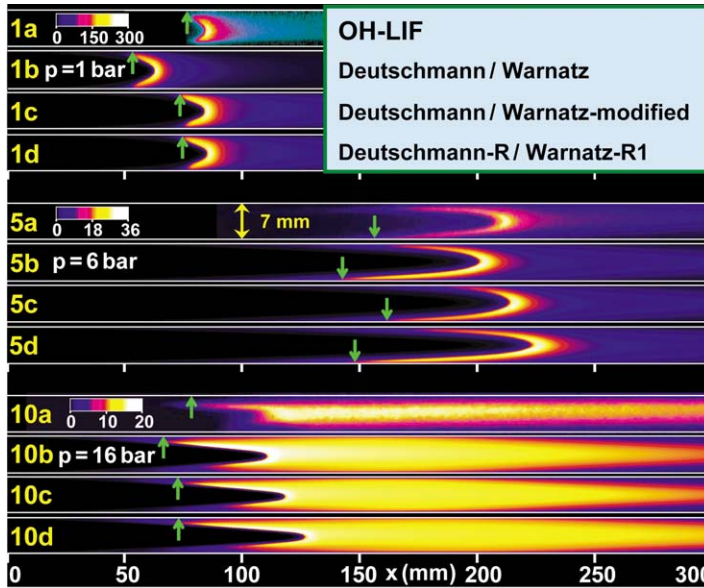


Fig. 12. Measured and predicted distributions of the OH radical for Cases 1, 5, and 10 of Table 1. (a) OH LIF measurements and (b–d) numerical predictions with: (b) Deutschmann/Warnatz schemes, (c) Deutschmann/Warnatz-modified schemes, (d) Deutschmann-R/Warnatz-R1 reduced schemes (see Tables 2 and 4). The green arrows define the onset of homogeneous ignition. The color bars provide the OH levels (ppmv) for both the experiments and the Deutschmann/Warnatz predictions.

Table 3

Kinetic parameters of the reaction $\text{CHO} + \text{M} = \text{CO} + \text{H} + \text{M}^a$

	A	b	E
Warnatz [22] (H_2)	$7.10\text{E}+14$	0.0	70.3
Warnatz-Maas [21] (H_2)	$7.10\text{E}+14$	0.0	70.3
GRI-3.0 [35] (N_2)	$1.87\text{E}+17$	-1.0	71.1
Leeds [36] (H_2)	$4.49\text{E}+14$	0.0	65.9
Friedrichs [46] (Ar)	$4.00\text{E}+13$	0.0	65.0

^a Reaction rate $k = AT^b \exp(-E/RT)$. Units A ($\text{cm}^3 \text{mol}^{-1} \text{s}^{-1}$), E (kJ/mol). The bath gas in the original kinetic measurements is shown in parentheses. The enhanced third-body efficiencies in the schemes of Warnatz, Warnatz-Maas and Leeds are $/\text{N}_2$ 0.4/ H_2O 6.5/ CO_2 1.5/ CH_4 3.0/ O_2 0.4/ CO 0.75/, while in GRI-3.0 are $/\text{H}_2\text{O}$ 6.0/ CO_2 2.0/ CH_4 2.0/ CO 1.5/.

of Fig. 12 (1a, 1c). Moreover, the already good performance of Warnatz' scheme in the range $6 \text{ bar} \leq p \leq 16 \text{ bar}$ ($\Delta x_{\text{ig}} \leq 9\text{--}15\%$) was further improved with the Warnatz-modified scheme ($\Delta x_{\text{ig}} \leq 3\text{--}8\%$) as seen in Fig. 12 (5a, 5c) and (10a, 10c).

4.5. Reduced homogeneous reaction schemes

It is a main interest to provide a reduced skeletal mechanism based on the validated Warnatz-modified scheme. The reduced mechanism should reproduce a variety of combustion characteristics such as ignition

delay times, catalytic and gaseous methane conversion, minor species concentrations over the induction zone, and onset of homogeneous ignition. For this purpose, a number of reactors were used: the ideal batch reactor, the ideal hetero/homogeneous SPSR, and, finally, the hetero/homogeneous channel reactor of the present study. Combining sensitivity and reaction flux analyses, a simplified mechanism was derived by eliminating the unimportant reactions and pathways. The thus derived skeletal mechanism, further denoted as Warnatz-R1, is provided in Table 4; it consisted of 28 reactions and 23 species and its range of applicability was $1 \text{ bar} \leq p \leq 16 \text{ bar}$, $900 \text{ K} \leq T \leq 1400 \text{ K}$, and $0.05 \leq \varphi \leq 0.5$. In Warnatz-R1, the kinetic parameters of the 28 reactions were those of Warnatz-modified (i.e., of Warnatz et al. [22] with the exception of R5). A smaller version of Warnatz-R1, further denoted as Warnatz-R2, composed of 23 reactions (R1–R23 in Table 4) and 18 species was also constructed for higher pressures and was applicable at $6 \text{ bar} \leq p \leq 16 \text{ bar}$, $1000 \text{ K} \leq T \leq 1400 \text{ K}$, and $0.05 \leq \varphi \leq 0.5$. Warnatz-R2 did not include the pathway $\text{CH}_3 \rightarrow \text{CH}_3\text{OH} \rightarrow \text{CH}_2\text{OH} \rightarrow \text{CH}_2\text{O}$ which, as stated in Section 4.3, was nonnegligible at lower pressures and temperatures.

Ignition delay times (constant pressure and temperature simulations, Eqs. (13)) with the Warnatz-modified, Warnatz-R1, and Warnatz-R2 schemes are depicted in Fig. 13 for three pressures. Predicted ignition delay times with the Warnatz-R1 scheme

Table 4
Reduced homogeneous reaction schemes^a

		A	b	E
R1	$O_2 + H = OH + O$	8.70E+13	0.0	60.3
R2	$HO_2 + OH = H_2O + O_2$	6.00E+13	0.0	0.0
R3	$H+O_2 + M = HO_2 + M$	2.30E+18	-0.8	0.0
R4	$CH_3 + O_2 \rightarrow CH_2O + OH$	3.30E+11	0.0	37.4
R5	$CHO + M = CO + H + M$	3.94E+14	0.0	70.3
R6	$CH_4 + OH = H_2O + CH_3$	1.60E+07	1.8	11.6
R7	$CO + OH = CO_2 + H$	4.76E+07	1.2	0.29
R8	$CH_3 + HO_2 = CH_3O + OH$	1.80E+13	0.0	0.0
R9	$CHO + O_2 = CO + HO_2$	3.00E+12	0.0	0.0
R10	$CH_3 + HO_2 = CH_4 + O_2$	3.60E+12	0.0	0.0
R11	$CH_3O + O_2 = CH_2O + HO_2$	4.00E+10	0.0	8.9
R12	$OH + OH = H_2O + O$	1.50E+09	1.1	0.42
R13	$HO_2 + HO_2 = H_2O_2 + O_2$	2.50E+11	0.0	-5.2
R14	$OH + OH + M = H_2O_2 + M$	3.25E+22	-2.0	0.0
R15	$CO + HO_2 = CO_2 + OH$	1.50E+14	0.0	98.7
R16	$CH_2O + H = CHO + H_2$	2.30E+10	1.1	13.7
R17	$CH_2O + OH = CHO + H_2O$	3.40E+09	1.2	-1.9
R18	$CH_2O + HO_2 = CHO + H_2O_2$	3.00E+12	0.0	54.7
R19	$CH_2O + O_2 = CHO + HO_2$	6.00E+13	0.0	170.7
R20	$CH_3 + CH_3 = C_2H_6$	8.32E+43	-9.1	67.0
R21	$CH_4 + O = OH + CH_3$	6.92E+08	1.6	35.5
R22	$CH_4 + HO_2 = H_2O_2 + CH_3$	1.10E+13	0.0	103.1
R23	$CH_3O + CH_3O \rightarrow CH_3OH + CH_2O$	3.00E+13	0.0	0.0
R24	$CH_2O + CH_3O \rightarrow CH_3OH + CHO$	6.00E+11	0.0	13.8
R25	$CH_3O_2 + M \rightarrow CH_3 + O_2 + M$	7.24E+16	0.0	111.1
R26	$CH_3 + O_2 + M \rightarrow CH_3O_2 + M$	1.41E+16	0.0	-4.6
R27	$CH_3O_2 + HO_2 \rightarrow CH_3O_2H + O_2$	4.60E+10	0.0	-10.9
R28	$CH_3OH + OH = CH_2OH + H_2O$	1.00E+13	0.0	7.1

^a The reduced schemes Warnatz-R1 and Warnatz-R2 consist of reactions R1–R28 and R1–R23, respectively. The kinetic parameters are the same as in Warnatz [22], with the exception of reaction R5 where the preexponential A has been reduced by a factor of 1.8. Reaction rate coefficient $k = AT^b \exp(-E/RT)$. Units A (cm-mol-K-s), E (kJ/mol). Enhanced third-body efficiencies: /CH₄ 3.0/CO₂ 1.5/CO 0.75/N₂ 0.4/O₂ 0.4/H₂O 6.5/H₂ 1.0/.

were within 20% to those of the Warnatz-modified mechanism for $T \leq 1300$ K and all pressures. At $T = 1400$ K the differences were somewhat larger (up to 26%); it is noted, however, that in practical systems temperatures as high as 1400 K were not representative of the bulk gas temperature but only of the catalyst. Warnatz-R2 has also provided, over its range of applicability ($p \geq 6$ bar, $T \geq 1000$ K), good agreement (within 25%) to the Warnatz-modified scheme predictions. Additional constant-pressure and constant-enthalpy simulations (Eqs. (13) and (14)) have shown that both reduced schemes captured well the ignition delay times of the Warnatz-modified scheme, indicating that the weak exothermicity over the induction zone was also well-reproduced.

In the next step, SPSR calculations (at given reactor pressures and temperatures, Eqs. (11)) were carried out in order to introduce coupling of the heterogeneous and homogeneous chemistries. Computed fractional methane conversions of both catalytic (C) and gaseous (G) pathways are provided in Fig. 14 for $p = 10$ bar, three surface to volume ratios, and

two residence times. The employed residence times (5 and 30 ms) bounded those of most practical devices and the variation in S/V determined the relative importance of each pathway. The predictions of Fig. 14 referred to the Deutschmann/Warnatz-modified, Deutschmann/Warnatz-R1, and Deutschmann-R/Warnatz-R1 schemes. The comparisons of Fig. 14 illustrated that the Deutschmann/Warnatz-R1 scheme provided good agreement (within 10%) to the CH₄ conversions of the Deutschmann/Warnatz-modified scheme over the entire examined range of parameter variation. In addition, the Deutschmann-R/Warnatz-R1 predictions were within 9% of those of the Deutschmann/Warnatz-R1 scheme. Minor species concentrations were also well predicted by the Warnatz-R1 scheme, as shown in Fig. 15. The level of agreement shown in Figs. 14 and 15 was preserved over the ranges $1 \text{ bar} \leq p \leq 16$ bar and $0.05 \leq \varphi \leq 0.5$. A similar outcome was reached for the performance of Warnatz-R2 (with the Deutschmann or the Deutschmann-R schemes) over its range of applicability.

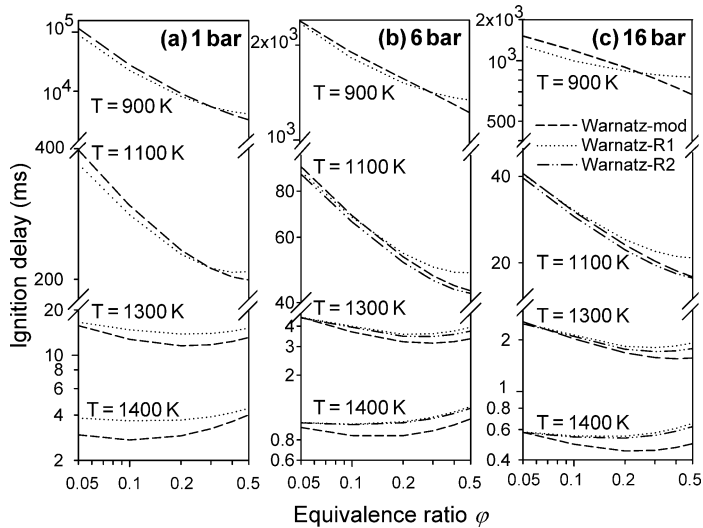


Fig. 13. Ignition delay times of CH_4/air mixtures at fixed pressures and temperatures calculated using the Warnatz-modified scheme (dashed lines), and the reduced mechanisms (see Table 4) Warnatz-R1 (dotted lines) and Warnatz-R2 (dashed-dotted lines). At $p = 1$ bar and all temperatures as well as at $T = 900$ K and all pressures, only Warnatz-R1 is relevant.

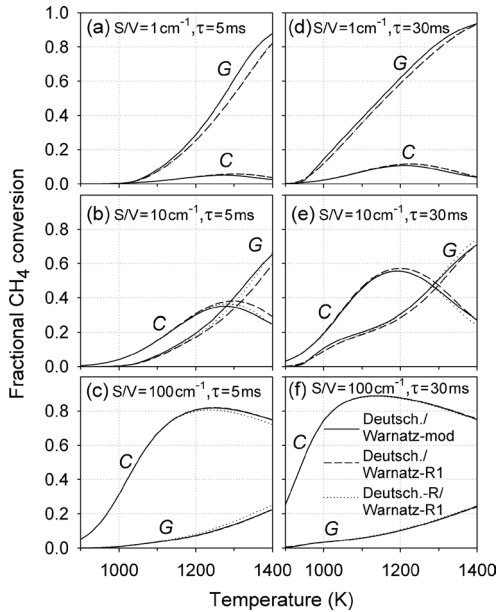


Fig. 14. Surface perfectly stirred reactor (SPSR) predictions of the fractional catalytic (C) and gaseous (G) methane conversion for a CH_4/air mixture with $\phi = 0.50$, $p = 10$ bar, three surface to volume ratios (S/V) and two residence times (τ). Solid lines: Deutschmann/Warnatz-modified schemes. Dashed lines: Deutschmann/Warnatz-R1 schemes (see Table 4). Dotted lines: Deutschmann-R/Warnatz-R1 schemes (see Tables 2 and 4).

The performance of the reduced gaseous mechanisms in the channel-flow experiments is finally illustrated in Fig. 12. Therein, comparisons between mea-

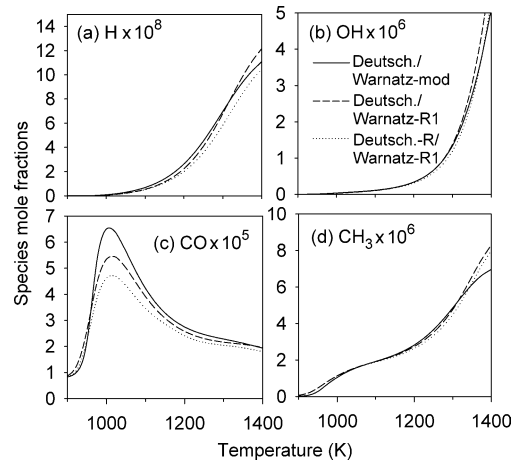


Fig. 15. Surface perfectly stirred reactor (SPSR) predictions of minor species mole fractions for a CH_4/air mixture with $\phi = 0.50$, $p = 10$ bar, surface to volume ratio $S/V = 10 \text{ cm}^{-1}$, and residence time $\tau = 30$ ms. Solid lines: Deutschmann/Warnatz-modified schemes. Dashed lines: Deutschmann/Warnatz-R1 schemes. Dotted lines: Deutschmann-R/Warnatz-R1 schemes (Tables 2 and 4).

sured (1a, 5a, 10a) and predicted with the Deutschmann-R/Warnatz-R1 schemes (1d, 5d, 10d) OH distributions illustrated that the Warnatz-R1 scheme reproduced very well (within 10%) the measured homogeneous ignition distance over the entire range $1 \text{ bar} \leq p \leq 16 \text{ bar}$. The combination of Warnatz-R1 with the full mechanism of Deutschmann (not shown) gave results similar to those of Deutschmann-R/Warnatz-R1. Moreover, the postignition flame

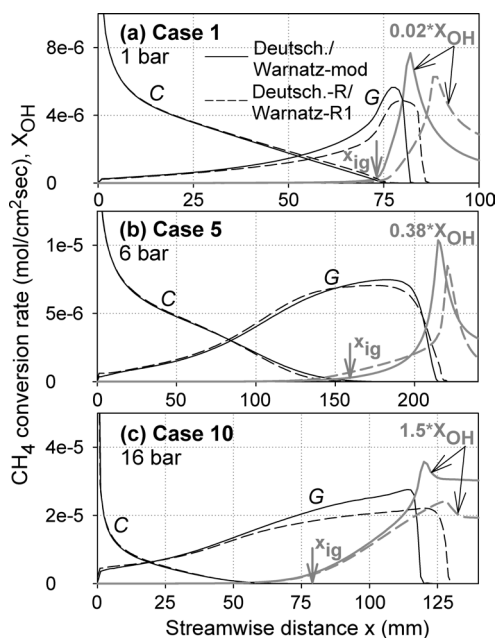


Fig. 16. Computed streamwise profiles of the catalytic (C) and gaseous (G) methane conversion rates and of the average (over the transverse distance) mole fraction of OH for three cases of Table 1. Solid lines: Deutschmann/Warnatz-modified schemes. Dashed lines: Deutschmann-R/Warnatz-R1 schemes (Tables 2 and 4).

shapes were also well reproduced by the Deutschmann-R/Warnatz-R1 schemes, although the flame tail lengths were somewhat overpredicted (compare Fig. 12 (10c and 10d)). This suggested that the reduced gaseous scheme underpredicted slightly the propagation characteristics (flame speeds). The predicted catalytic (C) and gaseous (G) methane conversion rates and the average (over y) OH mole fraction for the three cases of Fig. 7 are provided in Fig. 16; the volumetric G rates have been integrated over the 7-mm transverse channel distance so that they can be directly compared to the catalytic surface rates. The agreement between the Deutschmann/Warnatz-modified and Deutschmann-R/Warnatz-R1 predictions over the induction zone ($x \leq x_{ig}$) was good; the rise of the OH radical was somewhat slower in the reduced schemes, leading to the aforementioned slightly longer flame tails in Fig. 12. It is nevertheless emphasized that of main interest is the performance of the reduced scheme over the induction zone and its capacity to capture (for safety reasons) the onset of homogeneous ignition; the postignition flame propagation in the channel is less important since practical systems are not designed to operate in this mode.

As illustrated in Fig. 16, the gaseous pathway had a significant contribution to the conversion of methane well upstream of the onset of homogeneous

ignition. Furthermore, this contribution was more pronounced at higher pressures. The gas-phase impact is elaborated with the hetero/homogeneous carbon reaction flux analysis of Fig. 17, which was carried out with the Deutschmann-R/Warnatz-R1 schemes in an SPSR (the full Deutschmann/Warnatz-modified schemes gave essentially the same results). It is seen that CH_4 followed the gaseous route to CO and then most of the formed CO was adsorbed very efficiently on the surface due to its very high sticking coefficient (see S13 in Table 2). The adsorbed CO was oxidized to $\text{CO}_2(\text{s})$ that further desorbed via S10 to the gas phase. Considering that the gaseous combustion of hydrocarbons can be roughly described by a two-step process, the first being an incomplete reaction to CO and the second the oxidation of CO to CO_2 , it is clear that the presence of the catalytic pathway inhibited homogeneous ignition by depriving CO from the gas phase. Therefore, even in the absence of homogeneous ignition, the gaseous pathway could amount to significant methane conversion in high-pressure catalytic combustion systems. Although the catalytic pathway was an efficient sink of CO, it could not by itself provide acceptable CO emissions (20–50 ppmv): as seen in Fig. 7, CO dropped substantially only after the onset of homogeneous ignition. This was one of the reasons for pursuing CST (catalytic combustion followed by a postcatalyst gaseous zone) in gas turbines [1,2].

The impact of the heterogeneous scheme on homogeneous ignition was also addressed with sensitivity analyses. The preexponentials of all surface reactions in the Deutschmann-R scheme were multiplied/divided by a factor of 10 and the channel simulations were repeated while keeping the Warnatz-R1 gaseous scheme unaltered. It was shown that the CH_4 adsorption (S1) and O_2 adsorption/desorption (S2, S8) were particularly important as they determined the near-wall depletion of reactants. Radical adsorption/desorption reactions (S11, S12) had a smaller impact on homogeneous ignition [3,20]. Finally, the reduced gaseous schemes were largely independent of the particular catalyst and could thus be used in various hetero/homogeneous combustion applications.

5. Conclusions

The homogeneous ignition of fuel-lean ($0.31 \leq \phi \leq 0.40$) methane/air mixtures over platinum was investigated in the pressure range $1 \text{ bar} \leq p \leq 16 \text{ bar}$, which encompasses all practical catalytic combustion systems. In situ nonintrusive measurements of major species (using 1-D Raman) and trace species (using planar OH LIF) concentrations over the catalyst boundary layer of a channel-flow reactor were

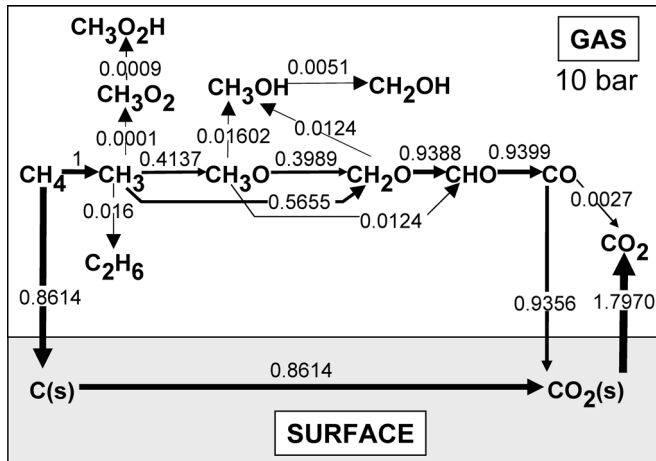


Fig. 17. Hetero/homogeneous reaction flux of carbon computed with the Deutschmann-R/Warnatz-R1 schemes (Tables 2 and 4) in a surface perfectly stirred reactor (SPSR) with a fuel-lean CH₄/air mixture ($\phi = 0.40$) at $p = 10$ bar and $T = 1200$ K. The surface to volume ratio was 5 cm^{-1} and the residence time 50 ms. All fluxes are normalized with respect to the CH₄ → CH₃ flux.

compared against detailed numerical predictions with elementary hetero/homogeneous chemical reaction schemes. The following are the key conclusions of this study.

1. The gas-phase mechanism of Warnatz reproduced well the measured homogeneous ignition distances over the range $6 \text{ bar} \leq p \leq 16 \text{ bar}$ and underpredicted them to a greater degree at $1 \text{ bar} \leq p \leq 4 \text{ bar}$. The gas-phase mechanisms of Leeds and GRI-3.0 underpredicted substantially the onset of homogeneous ignition at all pressures. Reaction flux analyses carried out over the temperature range $900 \text{ K} \leq T \leq 1400 \text{ K}$ (of interest to practical catalytic combustion systems) have shown that the scheme of Warnatz favored the low-temperature oxidation route $\text{CH}_3 \rightarrow \text{CH}_2\text{O}$, GRI-3.0 proceeded via the higher temperature route $\text{CH}_3 \rightarrow \text{CH}_3\text{O}$, and Leeds, although favoring the low-temperature route, had an increased contribution of the high-temperature pathway. It was also shown that crucial in the performance of the gaseous schemes was the correct prediction of the minimum equivalence ratio above which the self-inhibited ignition behavior of methane was maintained. Finally, notwithstanding the ultra fuel-lean conditions, C₂ chemistry could not be ignored. In particular, the inclusion of the radical recombination reaction $\text{CH}_3 + \text{CH}_3 = \text{C}_2\text{H}_6$ was necessary for accurate homogeneous ignition predictions.

2. Sensitivity analysis on the gas-phase scheme of Warnatz identified the importance and the strong pressure dependence of the chain-branching step $\text{CHO} + \text{M} = \text{CO} + \text{H} + \text{M}$ on homogeneous ignition. A reduction of the preexponential of this reaction by a factor of 1.8, which was further supported by recent kinetic studies, resulted in a gaseous scheme (modi-

fied scheme of Warnatz) that reproduced very well the measured homogeneous ignition characteristics over the entire pressure range $1 \text{ bar} \leq p \leq 16 \text{ bar}$.

3. Two skeletal reduced gas-phase mechanisms were derived from the modified scheme of Warnatz that reproduced a number of combustion characteristics: the ignition delay times in a batch reactor without surface reactions, the catalytic and the gaseous conversions in a surface perfectly stirred reactor, and, finally, the measured homogeneous ignition distances in the channel-flow catalytic combustor. The first reduced mechanism (Warnatz-R1) was established over the range $1 \text{ bar} \leq p \leq 16 \text{ bar}$, $900 \text{ K} \leq T \leq 1400 \text{ K}$, and $0.05 \leq \phi \leq 0.50$ and the second smaller mechanism (Warnatz-R2) was valid over $6 \text{ bar} \leq p \leq 16 \text{ bar}$, $1000 \text{ K} \leq T \leq 1400 \text{ K}$, and $0.05 \leq \phi \leq 0.50$.

4. When used in conjunction with a reduced heterogeneous scheme (based on the elementary scheme of Deutschmann), the reduced gas-phase mechanisms reproduced well the key catalytic and gaseous combustion characteristics of the full hetero/homogeneous mechanisms.

Acknowledgments

Support was provided by the Swiss Federal Office of Energy (BFE) and Alstom Power of Switzerland. We thank Dr. F. Raimondi and Ms. F. Geiger for the XPS and BET measurements.

References

- [1] R. Carroni, V. Schmidt, T. Griffin, *Catal. Today* 75 (2002) 287–295.

- [2] K.W. Beebe, K.D. Cairns, V.K. Pareek, S.G. Nickolas, J.C. Schlatter, T. Tsuchiya, *Catal. Today* 59 (2000) 95–115.
- [3] C. Appel, J. Mantzaras, R. Schaeren, R. Bombach, A. Inauen, B. Kaeppli, B. Hemmerling, A. Stambanoni, *Combust. Flame* 128 (2002) 340–368.
- [4] C. Appel, J. Mantzaras, R. Schaeren, R. Bombach, A. Inauen, N. Tylli, M. Wolf, T. Griffin, D. Winkler, R. Carroni, *Proc. Combust. Inst.* 30 (2005) 2509–2517.
- [5] M. Reinke, J. Mantzaras, R. Schaeren, R. Bombach, A. Inauen, S. Schenker, *Combust. Flame* 136 (2004) 217–240.
- [6] O. Deutschmann, L.I. Maier, U. Riedel, A.H. Stroeman, R.W. Dibble, *Catal. Today* 59 (2000) 141–150.
- [7] O. Deutschmann, R. Schmidt, F. Behrendt, J. Warnatz, *Proc. Combust. Inst.* 26 (1996) 1747–1754.
- [8] R.W. Sidwell, H. Zhu, R.J. Kee, D.T. Wickham, C. Schell, G.S. Jackson, *Proc. Combust. Inst.* 29 (2002) 1013–1020.
- [9] R.W. Sidwell, H. Zhu, R.J. Kee, D.T. Wickham, *Combust. Flame* 134 (2003) 55–66.
- [10] J.D. Taylor, M.D. Allendorf, A.H. McDaniel, S.F. Rice, *Ind. Eng. Chem. Res.* 42 (2003) 6559–6566.
- [11] J. Mantzaras, C. Appel, *Combust. Flame* 130 (2002) 336–351.
- [12] U. Dogwiler, J. Mantzaras, P. Benz, B. Kaeppli, R. Bombach, A. Arnold, *Proc. Combust. Inst.* 27 (1998) 2275–2282.
- [13] M. Reinke, J. Mantzaras, R. Schaeren, R. Bombach, A. Inauen, S. Schenker, *Proc. Combust. Inst.* 30 (2005) 2519–2527.
- [14] U. Dogwiler, P. Benz, J. Mantzaras, *Combust. Flame* 116 (1999) 243–258.
- [15] P.A. Bui, D.G. Vlachos, P.R. Westmoreland, *Proc. Combust. Inst.* 26 (1996) 1763–1770.
- [16] P. Markatou, L.D. Pfefferle, M.D. Smooke, *Combust. Sci. Technol.* 79 (1991) 247–268.
- [17] R.J. Cattolica, R.W. Schefer, *Combust. Sci. Technol.* 30 (1983) 205–212.
- [18] T.A. Griffin, L.D. Pfefferle, M.J. Dyer, D.R. Crosley, *Combust. Sci. Technol.* 65 (1989) 19–37.
- [19] L.D. Pfefferle, T.A. Griffin, M. Winter, D.R. Crosley, M.J. Dyer, *Combust. Flame* 76 (1989) 325–338.
- [20] M. Reinke, J. Mantzaras, R. Schaeren, R. Bombach, W. Kreutner, A. Inauen, *Proc. Combust. Inst.* 29 (2002) 1021–1029.
- [21] J. Warnatz, U. Maas, *Technische Verbrennung*, Springer-Verlag, New York, 1993.
- [22] J. Warnatz, R.W. Dibble, U. Maas, *Combustion, Physical and Chemical Fundamentals, Modeling and Simulation*, Springer-Verlag, New York, 1996, p. 69. Also available at: http://reaflow.iwr.uni-heidelberg.de/~ftp/reaflow/mechanism_for_export/Mech97.C1_C2_incl_thermodynamics.
- [23] C. Appel, J. Mantzaras, R. Schaeren, R. Bombach, A. Inauen, *Combust. Flame* 140 (2005) 70–92.
- [24] B. Steiner, Dissertation, Univ. of Stuttgart (2002).
- [25] S. Eisenberg, Diploma thesis, Univ. of Göttingen (1995).
- [26] A. Brockhinke, P. Andresen, K. Kohse-Höinghaus, *Appl. Phys. B* 61 (1995) 533–545.
- [27] R.J. Kee, G. Dixon-Lewis, J. Warnatz, M.E. Coltrin, J.A. Miller, A Fortran computer code package for the evaluation of gas-phase multicomponent transport properties, Report No. SAND86-8246, Sandia National Laboratories, 1996.
- [28] S.V. Patankar, *Numerical Heat Transfer and Fluid Flow*, Hemisphere, New York, 1980.
- [29] C. Appel, J. Mantzaras, R. Schaeren, R. Bombach, B. Kaeppli, A. Inauen, *Proc. Combust. Inst.* 29 (2002) 1031–1038.
- [30] J. Mantzaras, C. Appel, P. Benz, *Proc. Combust. Inst.* 28 (2000) 1349–1357.
- [31] H.K. Moffat, R.J. Kee, J.F. Grcar, J.A. Miller, Surface PSR: a Fortran program for modeling well-stirred reactors with gas and surface reactions, Report No. SAND91-8001, Sandia National Laboratories, 1993.
- [32] P. Glarborg, R.J. Kee, J.F. Grcar, J.A. Miller, PSR: a Fortran program for modeling well-stirred reactors, Report No. SAND86-8209, Sandia National Laboratories, 1996.
- [33] A.E. Lutz, R.J. Kee, J.A. Miller, SENKIN: a Fortran program for predicting homogeneous gas phase chemical kinetics with sensitivity analysis, Report No. SAND87-8248, Sandia national Laboratories, 1996.
- [34] J. Warnatz, M.D. Allendorf, R.J. Kee, M.E. Coltrin, *Combust. Flame* 96 (1994) 393–406.
- [35] Gas Research Institute, GRI Mechanism 3.0, 1999. Available at: http://www.me.berkeley.edu/gri_mech.
- [36] K.J. Hughes, T. Turányi, A. Clague, M.J. Pilling, *Int. J. Chem. Kinet.* 33 (2001) 513–538. Available at: <http://www.chem.leeds.ac.uk/Combustion/methane.htm>.
- [37] R.J. Kee, F.M. Rupley, J.A. Miller, Chemkin II: a Fortran chemical kinetics package for the analysis of gas-phase chemical kinetics, Report No. SAND89-8009B, Sandia National Laboratories, 1996.
- [38] M.E. Coltrin, R.J. Kee, F.M. Rupley, Surface Chemkin: a Fortran package for analyzing heterogeneous chemical kinetics at the solid surface–gas phase interface, Report No. SAND90-8003C, Sandia National Laboratories, 1996.
- [39] W.C. Pfefferle, L.D. Pfefferle, *Prog. Energy Combust. Sci.* 12 (1985) 25–41.
- [40] J. Mantzaras, P. Benz, *Combust. Flame* 119 (1999) 455–472.
- [41] L.J. Spadaccini, M.B. Colket, *Prog. Energy Combust. Sci.* 20 (1994) 431–460.
- [42] I. Glassman, *Combustion*, third ed., Academic Press, London, 1996, p. 91.
- [43] D.L. Baulch, C.J. Cobos, R.A. Cox, P. Frank, G. Hayman, T. Just, J.A. Kerr, T. Murrells, M.J. Pilling, J. Troe, R.W. Walker, J. Warnatz, *Combust. Flame* 98 (1994) 59–79.
- [44] R.S. Timonen, E. Ratajczak, D. Gutman, A.F. Wagner, *J. Phys. Chem.* 91 (1987) 5325–5332.
- [45] P. Glarborg, M.U. Alzueta, K. Kjaergaard, K. Dam-Johansen, *Combust. Flame* 132 (2003) 629–638.
- [46] G. Friedrichs, J.T. Herbon, D.F. Davidson, R.K. Hanson, *Phys. Chem. Chem. Phys.* 4 (2002) 5778–5788.